CrossMark

Combined high-resolution aeromagnetic and radiometric mapping of uranium mineralization and tectonic settings in Northeastern Nigeria

A. A. Adepelumi[1] · A. H. Falade[1]

Abstract Geological lineaments, depths to the basement, uranium concentrations, and remobilization in parts of the Upper Benue Trough, covering about 55×55 km^2 (longitudes 11°30′–12°00′E and 10°30′–10°30′N), Northeastern Nigeria were investigated using integrated High-Resolution Aeromagnetic Data (HRAD) and radiometric data. This was with a view to identifying the potential zones of uranium occurrence in the area. The HRAD was processed to accentuate anomalies of interest and depths estimate of 150–1941 m were obtained from source parameter imaging technique. The results from the superposition of the horizontal gradient magnitude, analytical signal amplitude, first vertical derivative, and 3D Euler solutions of the HRAD revealed that the study area was dissected by linear structures that trend ENE–WSW, NE–SW, E–W, NNE–SSW, WNW–ESE, and NW–SE; among which the ENE–WSW and NE–SW trends dominated. Analyses of radiometric data showed that uranium ores in the study area were possibly remobilized epigenetically from the granitic rocks, and were later deposited into sedimentary rocks (Bima formation). Burashika group (Bongna hills) and Wawa area of the study area showed vein-type deposits, while the anatectic migmatite in the northeastern region and the uranium rich Bima formation showed both fault/fracture and contact types of deposition. It was also observed the northwesterly and southeasterly, dominant dip direction, dipping faults dip in the same direction as the paleocurrent direction (direction of depositions of sediments), and trend in a direction perpendicular to the hypothetical direction of uranium deposition. The study concluded that the studied area is dissected by several linear structures and the studied area possibly contains deposits of uranium ore, which are likely to be found in: the Bima Sandstones of Wade, Shinga, Bima hill, Wuyo, Teli, Bryel, Dali, Barkan, Gasi, Kunkun, Boragara, Deba, and Gberundi localities; the anatectic migmatite at Kubuku, Whada, and Hyama; and the Bongna hills and agglomerates around Burashika, Kawaba, and Galu.

Keywords Uranium · Radiometric · Aeromagnetic · Sandstone · Fault · Vein deposit

Introduction

Epileptic power supply has been of constant increase in Nigeria due to consistent increase in energy demand. In 2001, electricity generation went down from the installed capacity of about 5600 MW to an average of about 1750 MW, as compared to a load demand of 6000 MW (Sambo 2008). In addition, energy demand was projected to rise from 5746 MW in 2005 to 297,900 MW in the year 2030, which translates to construction of 11,686 MW every year to meet this demand (Sambo 2008). To meet this demand, nuclear energy is consistently being mentioned in government circles, but it is not optimistic at present. However, it may be adopted in the near future.

Uranium, being the principal fuel for world's nuclear plants, has become a valuable source of energy in many countries (Tauchid 1993). It is a very dense (19 g cm^{-3}) radioactive metallic element with an abundance of energy. Economical deposition of uranium can be found in a variety of rocks and the solubility of uranium in water has

✉ A. A. Adepelumi
aadepelu@oauife.edu.ng; adepelumi@gmail.com

[1] Geology Department, Obafemi Awolowo University, Ile-Ife, Nigeria

enhanced its deposition and also accounts for its presence in surface water, ground water, and sea. In Nigeria, significant uranium occurrence was noted during the 1976–1983 search period. The ignimbrite field in Niger was observed, and the significant radiometric anomaly was shown with an unidentified source (Bowden et al. 1981). Further search that was conducted in Zona, Northeastern Nigeria, between years 1995 and 2000 revealed the Precambrian basement/Cretaceous sediment unconformity uraniferous anomaly in the area (Suh et al. 1998). Other radiometric anomalies were seen in Mika and Ghumchi, with their sources traced to granitic bodies (Maurin and Lancelot 1990; Funtua and Okujeni 1996; Suh and Dada 1998). This uranium anomaly revealed in Zona is arguably the most significant sandstone hosted Uranium deposition in Northeastern Nigeria (Suh et al. 1998). The host rocks are fluvial arkosic sandstones (Bima sandstone formation) interbedded in places with silty lenses and mudstones and occupying a more or less N 65 E trending structural basin (Suh et al. 1998).

Hence, the Upper Benue Trough of the Northeastern Nigeria has been chosen for this study to provide geophysical evidence of the deposition of uranium, analyse the tectonic settings, and map other areas suitable for uranium deposition in the area. Airborne magnetic and radiometric geophysical surveying methods, being the most commonly used methods for uranium exploration, will be adopted in this study.

Aeromagnetic survey technique is a powerful tool in delineating the regional geology (lithology and structure) of buried basement terrains (Gaafar and Aboelkhair 2014). This technique is used for detecting variation in geomagnetic field caused by changes in magnetic susceptibility of subsurface rocks due to changes in the percentage of grains of magnetic minerals forming these rocks. Variation in susceptibility assists in distinguishing various rock types; application of mathematical expressions on this helps in delineating some geological structures.

Airborne radiometric method has become a useful method, all over the world, in quest for uranium mineralization (Telford et al. 1990). The method utilizes a gamma ray spectrometer which measures the radioactivity emanating from the natural decay of elements such as potassium, uranium, and thorium from the earth surface. This tool, with shallow depth of penetration, has the special quality of distinguishing these decay elements from one another based on their energy level. Geological mapping and search for other mineral resources such as heavy minerals, beach sands, and phosphates can also be done using radiometric method (Foote and Humphrey 1976; Saunders and Potts 1976).

Geology of the study area

As shown in Fig. 1, the study area falls within the basement complex and sedimentary terrain of Nigeria. The basement complex terrain encompasses the Precambrian age rocks, which were classified, according to Carter et al. (1963), into Older granites and Burashika groups. The older granites are said to have emanated from the remnants of an ancient sedimentary series which have now transformed entirely into anatectic migmatites and granites (Carter et al. 1963). The older granites are distinguished into three phases; these are the basic and intermediate plutonic rocks, fine-grained granites (which form the earliest intrusions of the older granite orogeny), and syntectonic granites. The formation of Burashika group began, in the course of granitic dyke intrusion, after a considerable interval of the closure of the older granite orogeny. The formation led to magmatic activities which involved the intrusion of lavas and granites into the older granite. Sequential deposition of a great thickness of continental and marine sands and clays which are of Cretaceous-to-Paleocene age preceded after the formation of the Precambrian rocks.

This sequence of deposition forms the sedimentary terrain through which Bima sandstone, which unconformably overlaid the Precambrian rocks, formed the first set of the deposition. Upper Benue Trough is demarcated from Chad Basin by Zambuk Ridge. This area is entirely filled with Cretaceous right from the first formation on the crystalline basement, Bima formation, to the last formation and its lithostratigraphy is subdivided into two arms: the Gongola arm and the Yola arm. The Gongola arm of Upper Benue Trough is made up of five stratigraphic units which include the Bima sandstone at the bottom, Yolde formation, Pindiga formation, Gombe sandstone, and Keri–Keri formation, while that of Yola Arm include the Bima formation, Yolde formation, Dukul formation, Jessu formation, Sekule formation, Numanha formation, and the youngest, Lamja formation (Carter et al. 1963; Obaje 2009; Odebode 2010; Nwajide 2013).

Series of tectonic activities such as folds and fractures occurred in this area which led to the intrusion of volcanic plugs. The tertiary volcanic rocks that intruded these rocks are widely distributed across the study area; these rocks are grouped into three by Benkhelil (1986): basalt, phonolite, and trachyte. Earth movement of the late Cretaceous determined the structures of this area, but this ceased before the tertiary. The Paleocene and Younger strata are flat lying and unaffected by folding and faulting. Various fault trends are also present, but the dominant direction lies between NNE and ENE (Carter et al. 1963).
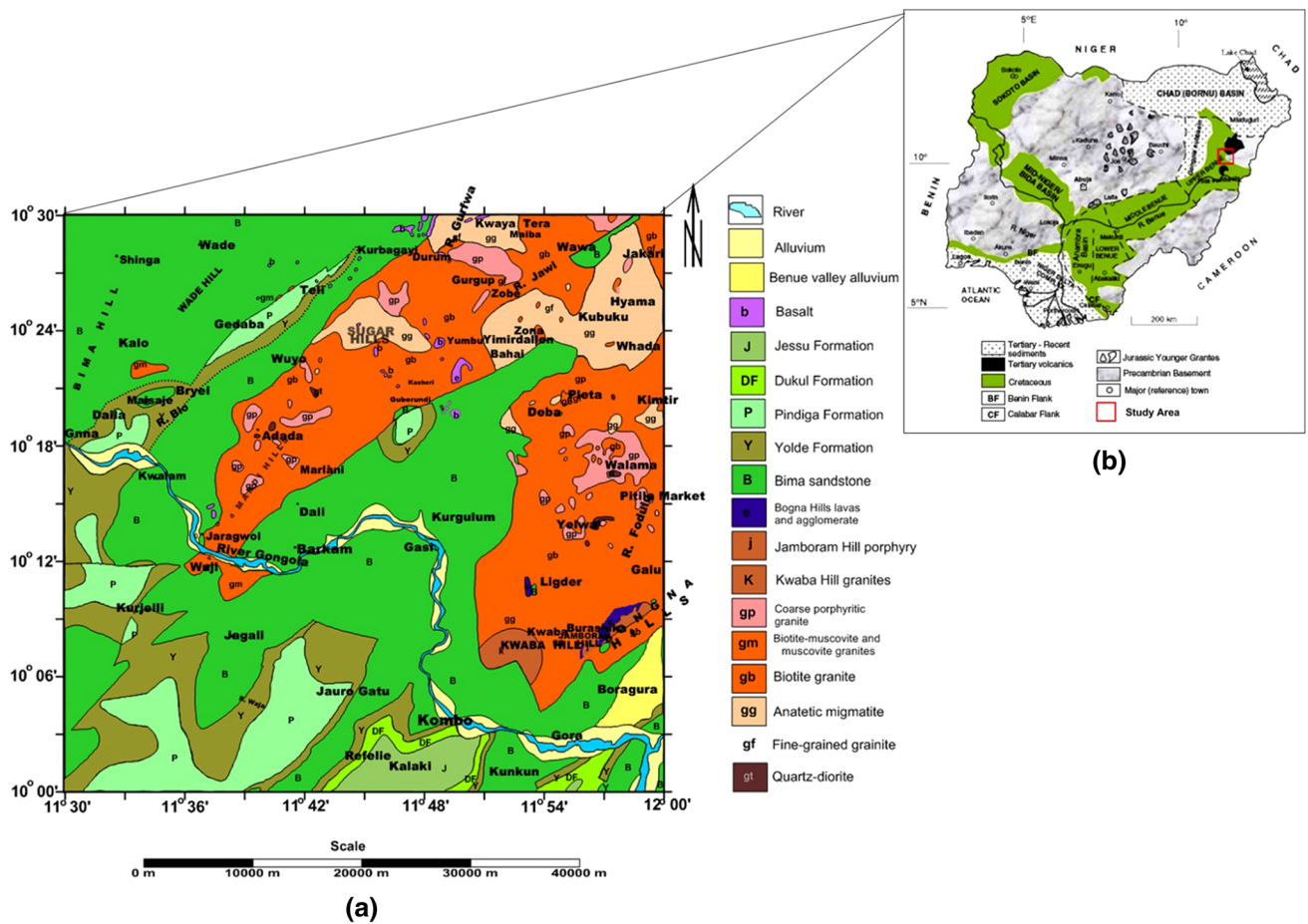
Fig. 1 **a** Geological map of the study area (modified from Carter et al. 1963); **b** Geological map of Nigeria showing the study area (modified from Obaje 2009)

Methodology

High-Resolution Aeromagnetic Data (HRAD) and airborne radiometric data (equivalent uranium and thorium data) of part of Northeastern Nigeria were acquired from the Nigeria Geological Survey Agency (NGSA). The data covered an area of about 55 × 55 km² (bounded by latitudes 10°00′–10°30′N and longitudes 11°30′–12°00′E). The aeromagnetic and radiometric surveys were carried out between 2003 and 2009 by Fugro Airborne Surveys for the NGSA. The data were recorded at an interval of 0.1 s (∼7.5 m) for magnetic measurements and 1.0 s (∼75 m) for radiometric measurements. The airborne surveys were flown in the NW–SE direction perpendicular to the major geological trends in the area, with flight line spacing of 500 m, terrain clearance of 80 m, and tie line spacing of 2000 m in NE–SW direction. Based on the very short recording interval, lower survey flight height (80 m), and narrower flight line spacing, the resolution of the anomalies is immensely higher than the conventional high-altitude air borne surveys. All essential data corrections, including the

removal of IGRF values, were done by Fugro Airborne Surveys.

The acquired magnetic and radiometric data were gridded at 100 m grid spacing, using minimum curvature technique, to produce the Total Anomaly Field (TAF) map and equivalent thorium and uranium maps. The 100 m grid spacing, which is one-fifth of the survey flight line spacing, was used to avoid short-wavelength errors which may appear as lines perpendicular to the survey flight line (Anudu et al. 2014). The chosen grid cell size also satisfies the opinion of Dentith (2011) that grid spacing should be between one-third and one-fifth of the survey flight line. The maps were processed using the Oasis Montaj software. The TAF map (Fig. 2) was reduced to the equator (Fig. 3a), using magnetic inclination (−2.33778°) and declination (−0.95732°) of the centre point of the study area, so that anomalies observed would be directly positioned on their respective causative source bodies. Unwanted signals which include the regional fields were removed by upward continuing the Reduced-to-Equator (RTE) map to a height of 2 km, where the resulted map
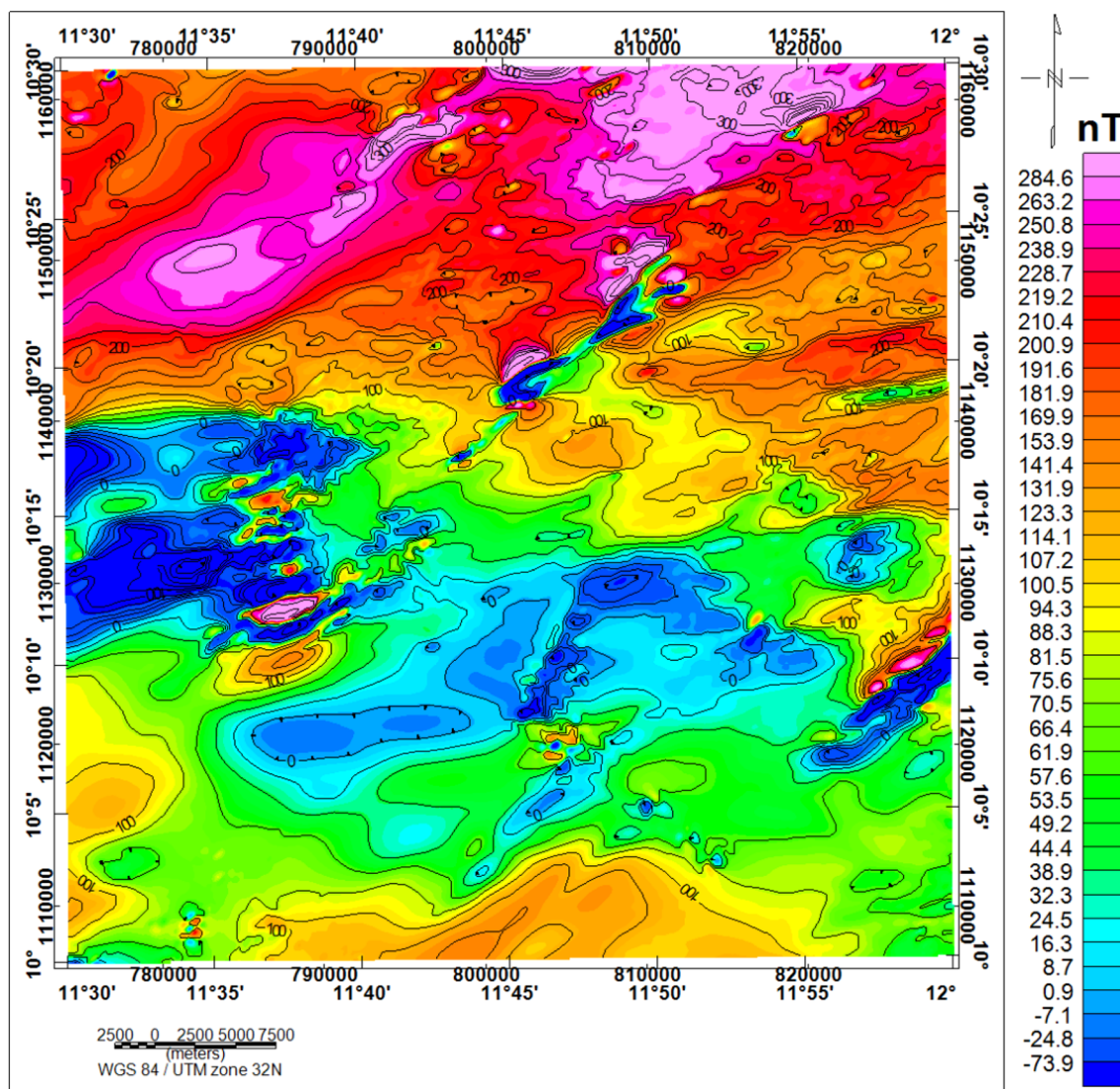
Fig. 2 Total anomaly field (TAF) map of the study area

was subtracted from the RTE map to obtain the residual map (Fig. 3b). This residual map was upward continued to a height of 200 m to remove responses from near surface cultural features. The upward continued residual map (Fig. 4a) was divided into nine overlapping blocks, which were subsequently subjected to spectral analysis. The results (magnetic source depths) obtained from the analysis of the radially averaged power spectrum of each block were compiled to produce the average depth map of the magnetic source layer in the study area. Horizontal Gradient Magnitude (HGM), First Vertical Derivative (FVD), and Analytical Signal (AS) source edge mapping techniques were applied on the filtered residual data to delineate the magnetic source boundaries. Euler Deconvolution (ED) method was also used to determine the geometry, location, and depth to the magnetic sources. More also, Source Parameter Imaging (SPI) technique was used to

determine depth to the magnetic source, and it was also used as constraint in 2D forward modelling. The radiometric data which comprise both the equivalent uranium and thorium maps (majorly used for uranium exploration) were displayed, and various ratios of these maps which include eU/eTh, eU^2/eTh, and eU–(eTh/3.5) (which have different geological meanings) were calculated using the Oasis Montaj Software. The geologic, aeromagnetic, and radiometric maps were correlated, and 2D forward modelling of some suspected profiles across the study area was carried out using the GM-SYS^{TM} module of the Oasis Montaj software to determine the variation in the geometry, depth, horizontal position, and magnitude of magnetization of the source body. Thereafter, environments and lineaments favourable for uranium deposit were deduced and interpreted accordingly.
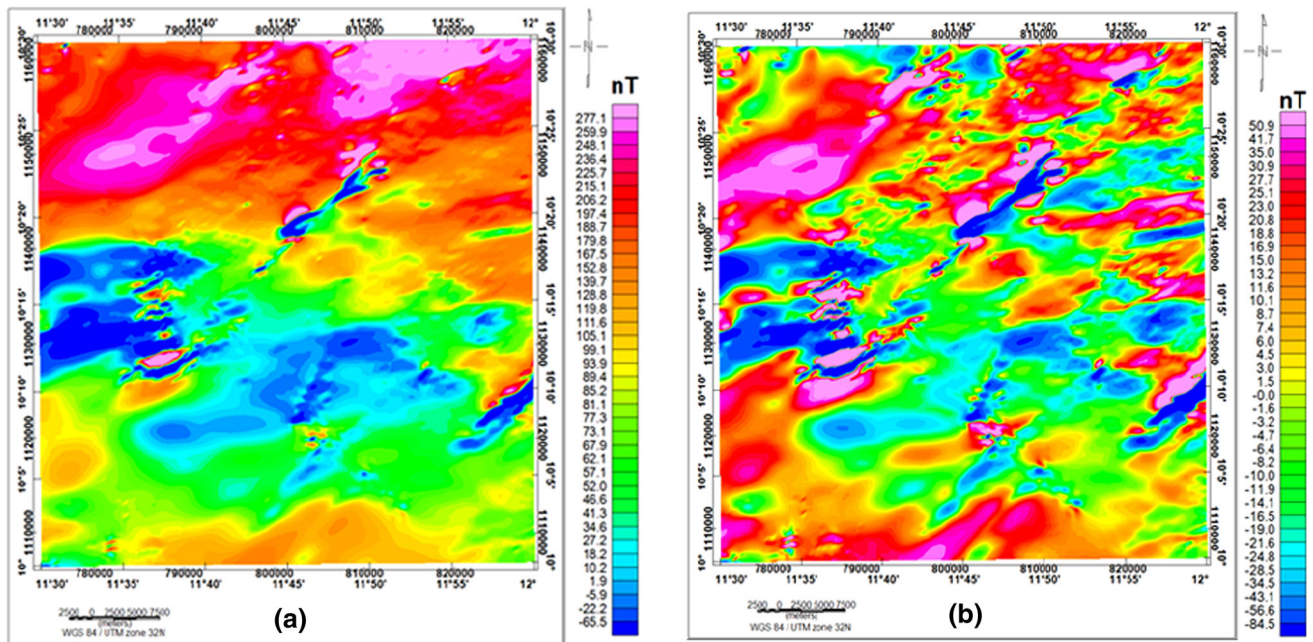
Fig. 3 **a** Reduction to the equator map of the TAF map; **b** residual map of the study area (obtained) from the removal of the regional field

Horizontal gradient of potential field anomalies is steepest approximately over edges of tabular sources (Dobrin and Savit 1988). The maxima of horizontal gradient are located at the edges of the tabular body and this can assist when inspecting for magnetization contrasts. HGM are used by some interpreters for mapping body outlines. The magnitude of the horizontal gradient of the RTP, RTE, or pseudogravity transformation of a gridded magnetic field data is given by

$$H(x,y) = \left[\left(\frac{\partial M}{\partial x} \right)^2 + \left(\frac{\partial M}{\partial y} \right)^2 \right]^{\frac{1}{2}}.$$

From the equation above, $\partial M / \partial x$ and $\partial M / \partial y$ are the field gradients in the x (East) and y (North) directions, respectively.

Vertical derivative enhances shallow features at the expense of anomalies caused by deeper sources. When vertical derivative is applied to magnetic data, it sharpens the edges of the magnetic sources. The equation of first derivative can be written as

$$\text{VD} = \frac{\partial M}{\partial z}.$$

In the equation above, VD is vertical derivative, and $\partial M / \partial z$ is the magnetic field in z direction.

Analytical signal shows an anomaly over a causative body which is independent of the directions of magnetization of the body, but on the location of the body itself. It has lower sensitivity to inclination of geomagnetic field which makes it effective for the transformation of the shape of magnetic anomaly from any magnetic inclination to one positive body-centred anomaly (Nabighian 1972). The amplitude of analytical signal can be derived from three orthogonal gradients of the total magnetic field according to Roest et al. (1992)

$$A(x,y) = \left[\left(\frac{\partial M}{\partial x} \right)^2 + \left(\frac{\partial M}{\partial y} \right)^2 + \left(\frac{\partial M}{\partial z} \right)^2 \right]^{\frac{1}{2}},$$

where $A(x, y)$ is the amplitude of the analytical signal at (x, y) and M is the observed magnetic anomaly at (x, y). Analytical signal, which peaks over the edges of source bodies, helps to reveal and highlight discontinuity using Hilbert transformation and Fourier transformation of the source field (Nabighian 1984).

Most processing algorithms proposed for the interpretation of magnetic data either estimate the depth or locate boundaries. However, Euler deconvolution is both a boundary finder and a depth estimator (Reid et al. 1990). It extracts information from grids using the homogeneity relation shown by Thompson (1982). This relation can be written in the form:

$$(x - x_0) \frac{\partial T}{\partial x} + (y - y_0) \frac{\partial T}{\partial y} + (z - z_0) \frac{\partial T}{\partial z} = N(B - T),$$

where (x_0, y_0, z_0) is the position of a magnetic source, whose total field T is detected at (x, y, z); B is the regional field value; and N is the degree of homogeneity interpreted as structural index (SI) (Thompson 1982), which is a measure of the rate of change with distance of a field, and this structural index is chosen based on the prior
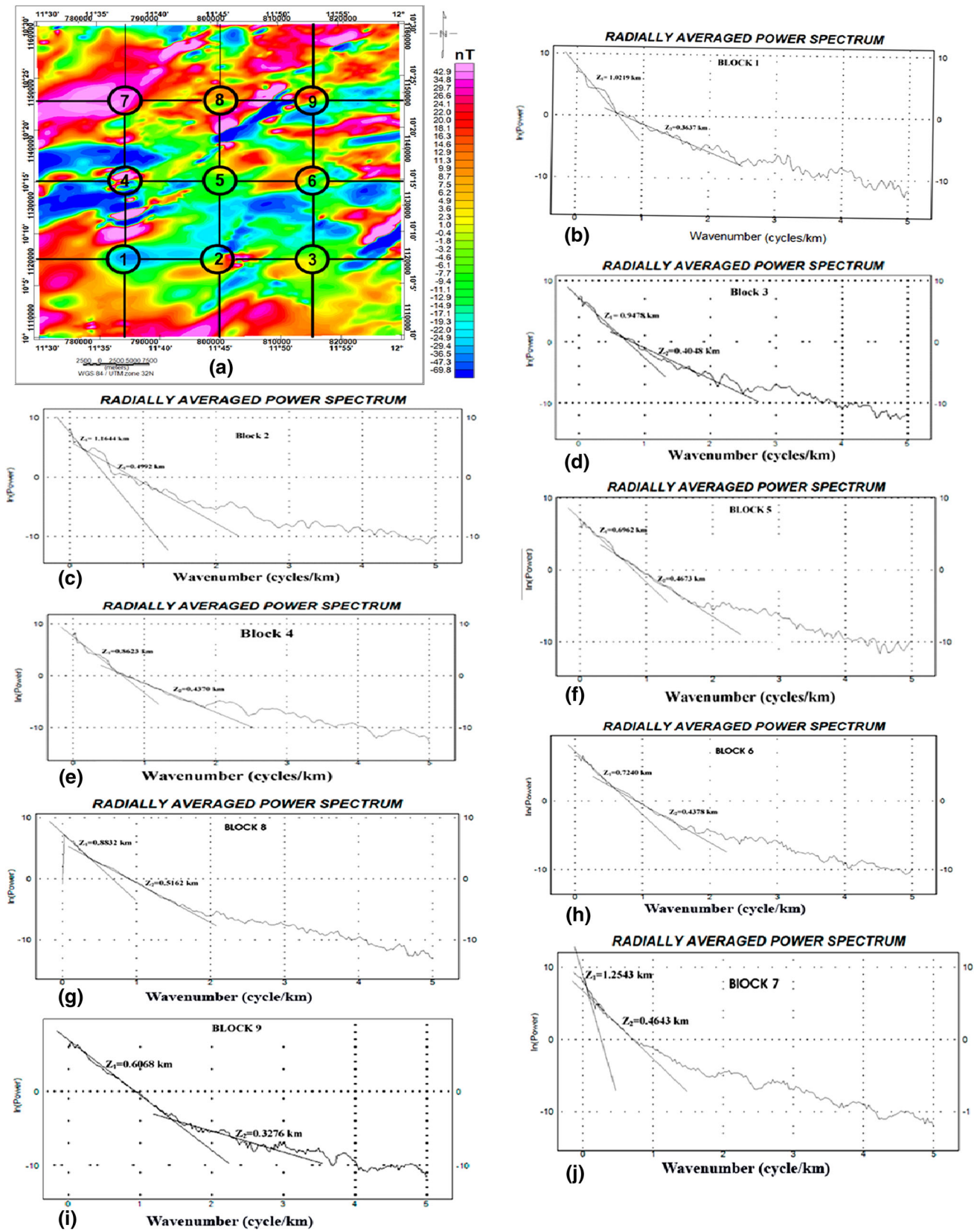
Fig. 4 a 200 m upward continuation map of the residual map—the super imposed numbers indicate the centre of the overlapping blocks; b–j radially averaged power spectrum of blocks 1–9

knowledge of the source geometry. SI varies from zero to three for different bodies ($N = 0$ for contacts, 1 for sill/dyke/fault, 2 for pipe/horizontal bodies, and 3 for spherical bodies, respectively) (Reid et al. 1990).

Source parameter imaging (SPI) is one of the methods used for the determination of depth to the magnetic basement that is beneath a sedimentary cover. This method sources its parameters from gridded data and uses an extension of complex analytical signal to estimate the magnetic source depth. The technique (sometimes referred to as the local wavenumber method) is a profile or grid-based method that estimates the magnetic source depth, dip, and susceptibility contrast of some source geometries (Thurston and Smith 1997; Thurston et al. 1999, 2000; Nwosu 2014).

Results and discussion

Qualitative interpretation of aeromagnetic maps

Qualitative interpretation of aeromagnetic data involves visual inspection of the map for recognition of zones with different magnetic characteristics, shapes, and trends. The study area, which covers both basement complex and sedimentary terrain, showed anomalies of various magnetic characteristics. This is as a result of the differences in the sizes, depths, and magnetic susceptibilities of the underlying rocks.

The basement complex zone of the study area is magnetically perturbed than the sedimentary zone because of the high sedimentary cover on the basement rocks. The TAF map (Fig. 2) shows high and low magnetic anomalies of various wavelengths. Most of the anomalies trend in the NE–SW direction, while others trend in the E–W and NW–SE directions. The magnetic intensity value of the study area varies from −74 to 285 nT. The upper region contains high magnetic intensities (114–284 nT), the central part is dominated by low magnetic intensities (−24–123 nT), while the magnetic intensities of the southern part are moderate (53–114 nT). The low magnetic intensity value observed within the magnetic high in the northern flank suggests the presence of deep-seated fault zone which trends in the same direction as the observed anomaly. The adjacent magnetic high and low anomalies at latitude 10°10′ (Fig. 2) of the southeastern part of the study area correspond to the Burashika group (Bongna hills lava and agglomerate and Jamboram hill porphyry) on the geological map.

Computation of residual

The residual and filtered residual maps are presented in Figs. 3b and 4a. The magnetic intensity of the filtered map

ranges between −70 and 43 nT. The E–W trending low amplitude anomalies observed at the western flank of the study area show the presence of rocks of high magnetic susceptibility in the area. Some intercalations of E–W and ENE–WSW trending magnetic highs, which are of shorter wavelengths, into the magnetic lows in the area indicate the presence of smaller and less magnetic rock bodies over or in between the rocks giving the low magnetic anomaly signature. The high amplitude anomalies observed at the northwestern and southern parts of this map may be due to the presence of low magnetic rocks (e.g., shale, sand, sandstone, mudstone, and limestone) present in the study area. In the lower part of the northeastern region of the map, a prominent low magnetic intensity value, which is tabular in shape and trends in the ENE–WSW direction, was observed in between magnetic highs; this anomaly is likely to be from a dyke-like structure, fault, or fracture. From the central part to the northeastern part of the study area, an elongated structure trending NE–SW which has been featuring in both the TAF map and filtered residual map is likely to be major fault/fracture hosting magnetic minerals, whose response results in the significant low anomaly amplitude in between the relatively high amplitude anomalies in the area.

## Quantitative interpretation of aeromagnetic data basement analysis

Magnetic basement average depth determination using spectral analysis

Figure 4 shows the subdivision of the filtered residual map into nine overlapping blocks and the radially averaged power spectrum of these nine blocks. In these plots, the log of energy reduces with increasing wavenumber. Since the effects from all physical sources (geology) contribute to any measurement taken in potential field, the energy spectrum clearly shows the ensemble of sources that contributed to the energy from low to high wavenumbers. In this study, the lower wavenumber sources which are the deep-seated sources are the sources of interest, and Table 1 shows the average depths estimated from each block.

The result obtained from the average power spectrum of these blocks, z_1, in Table 1 was used to generate the 2D and 3D depth maps (Fig. 5a, b). The 2D map shows the sedimentary thicknesses of the study area, while the 3D map shows the basement morphology of the area. On the 2D map (Fig. 5a), the hot colours (red and pink) correspond to shallow depths, while the cool colours (e.g., blue) correspond to deep depths. The basement topography map (Fig. 5b) shows that depths to the magnetic basement range from 650 to 1250 m below the surface. The elevated

Table 1 Estimated depths from radially averaged power spectrum of blocks 1–9

Blocks	1	2	3	4	5	6	7	8	9
Depth Z_1 (km)	1.0219	1.1644	0.9478	0.8623	0.6962	0.7240	1.2543	0.8832	0.6068
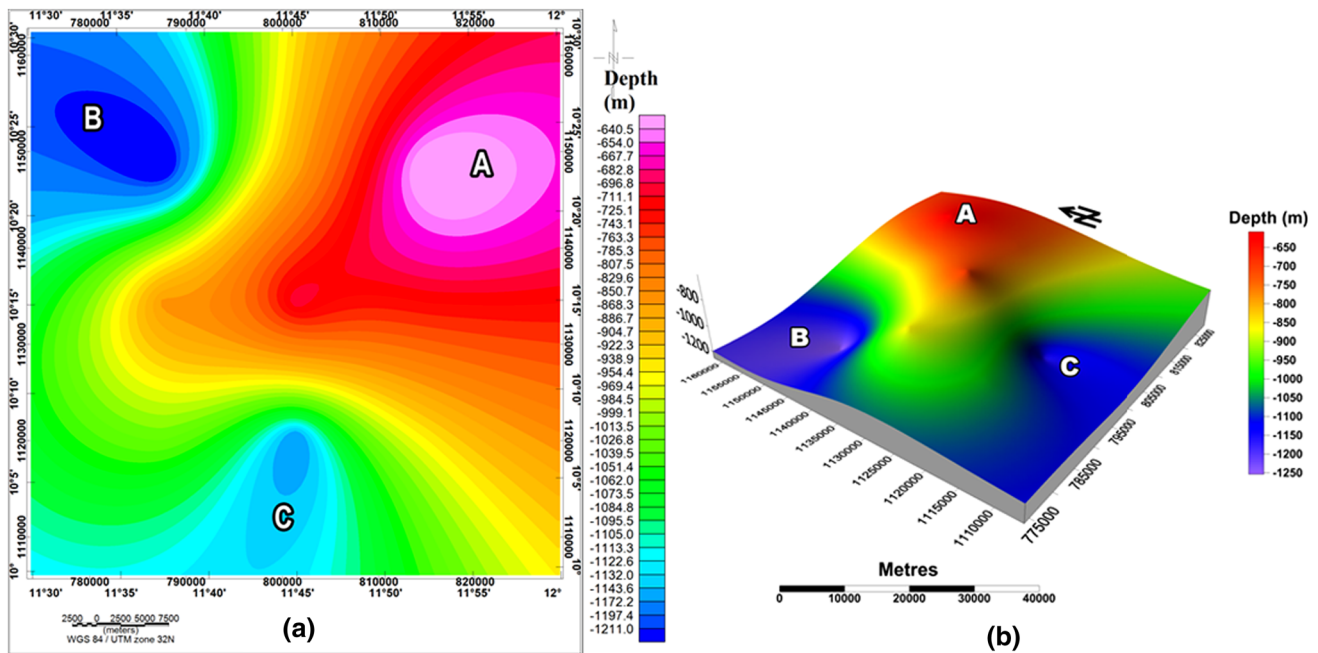
Fig. 5 **a** Depth to the basement (*sedimentary thickness*) map of the study area; **b** basement morphology map of the study area inferred from spectral analysis

portion of the map (labelled A) corresponds to the basement complex terrain that was observed on the geological map of the study area (Fig. 1), while the relatively deep regions (labelled B and C) mapped in the northwestern and southern parts of the study area correspond to the sedimentary terrains. Moderate depths were observed at the western flank.

Depth estimation using source parameter image (SPI)

The SPI map for the study area is shown in Fig. 6. The white portions on the map signify areas, where the derivative used for the estimation of the local wavenumber is so small that the SPI structural index cannot be estimated reliably. As shown on the SPI map, the depths to the magnetic basement vary from 150 to 1941 m. Some deep zones (>800 m) were observed in various parts of the map. The deep zones are more pronounced in the northwestern and southwestern parts of the study area, while those that are less pronounced (i.e., deep zones of very small width extent) were mapped in few parts of the upper diagonal of study area. The northeastern, central, and southeastern parts are dominated by shallow depths (<400 m) to the basement.

The SPI map correlates well with the spectral depth map (Fig. 5a, b). The northwestern and southwestern portions of the study area were also seen as depression or low-lying surface, while the northeastern, central, eastern, and southeastern portions are elevated. The difference in depth ranges obtained from the spectral method and the SPI is as a result of the average depths calculated from the spectral windows. The SPI generally gives a more localized estimation of depths than the power spectral and, therefore, shows a depth map of higher resolution. The results from both methods correlate with what was observed on the geological map. Areas with shallow depths correlate with basement complex terrain, whereas the high depth values correlate with sedimentary terrains.

Lineament mapping

Horizontal gradient magnitude (HGM) and analytical signal (AS) maps

As HGM peaks over the source edges, so does AS, but the shape of the analytic signal is independent on the direction of magnetization and local magnetic field. HGM map reveals that more structural complexities which include the
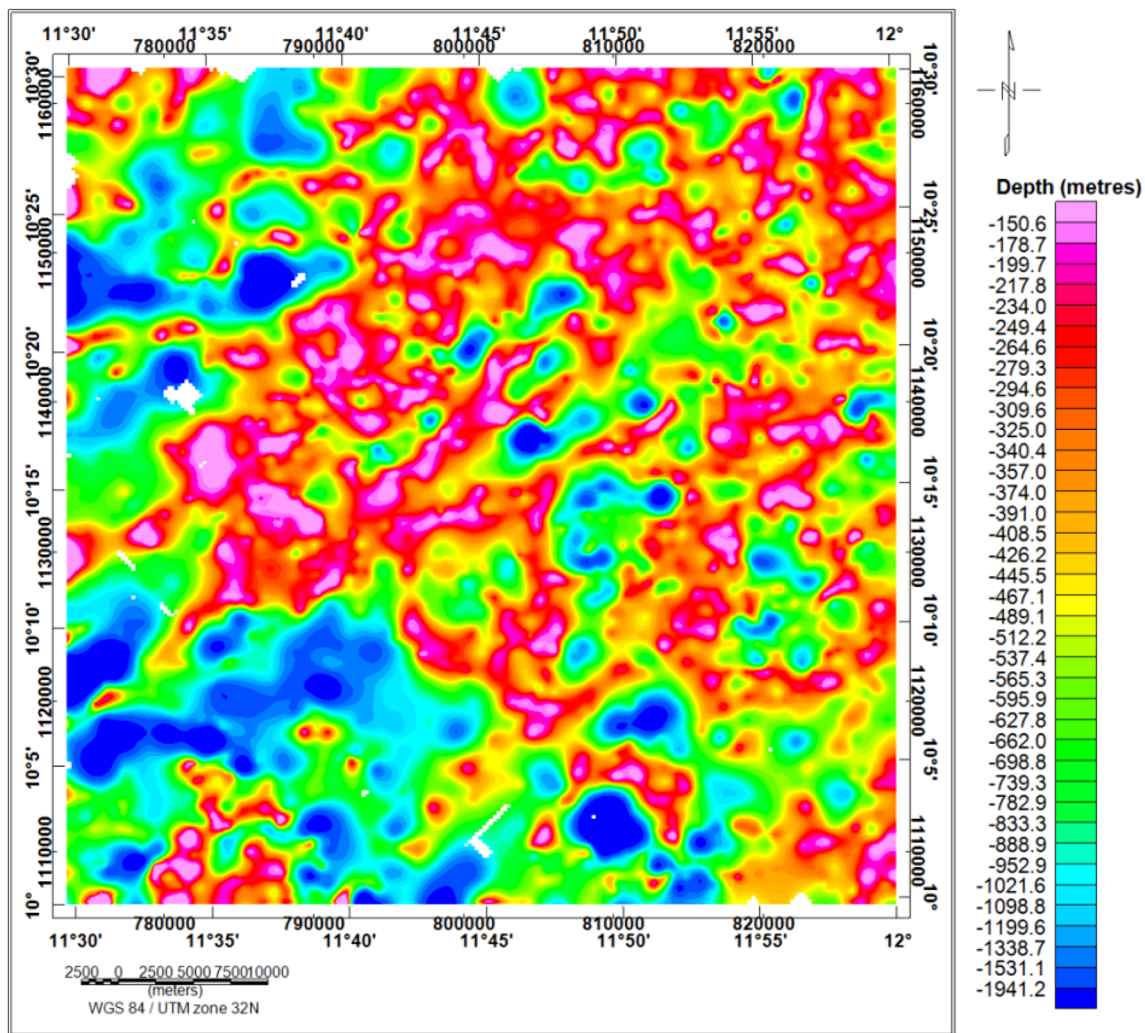
Fig. 6 Map showing the depth of magnetic source from source parameter imaging (SPI)

lithological contacts of various geological bodies than AS map and contacts produced in HGM maps, according to Philips (2000), are assumed to be dislocated in the down-dip direction for dipping contact sources. Figure 7 shows the locations of both HGM and AS maxima, respectively. From the maps, the maxima show contacts that trend mostly in the ENE–WSW, NE–SW, E–W, and NW–SE directions; among which, the ENE–WSW trends predominate.

Interpretation of 3D Euler deconvolution

According to Reid et al. (1990), magnetic contact has structural index of zero; however, real faults are typically complex structures, and the use of slightly higher indices is often appropriate. Therefore, to distinguish faults/fractures from lithological contacts in the study area, structural index of 1 was adopted. Figure 8 shows the Euler solution plot for structural index of 1. The depths were grouped every

500 m, and the result shows that faults/fractures existing between the depths of 500 and 1000 m dominate the study area. The result also shows prominent NE–SW, ENE–WSW, E–W, and NW–SE trending structures. A critical visual inspection of the faulting pattern indicated by the NE–SW trending alignments of many Euler solutions shows that the study area has been affected by an NE–SW trending regional fault system, whose history could be traced to the Pan African Orogeny. The Euler solutions show that the structures in the northwestern and southwestern portions of the study area exist at relatively deep depths than those in other parts. Linear clustering of different depth solutions indicates variation in depths along the fault zones. Many structures whose depths are greater than 1000 m featured in the northwestern and southwestern portions. Shallow solutions were observed from the central region to the northeastern part of the study area. These solutions, which are less than 1000 m in depth and trend in the NE–SW direction, also fall on the basement complex
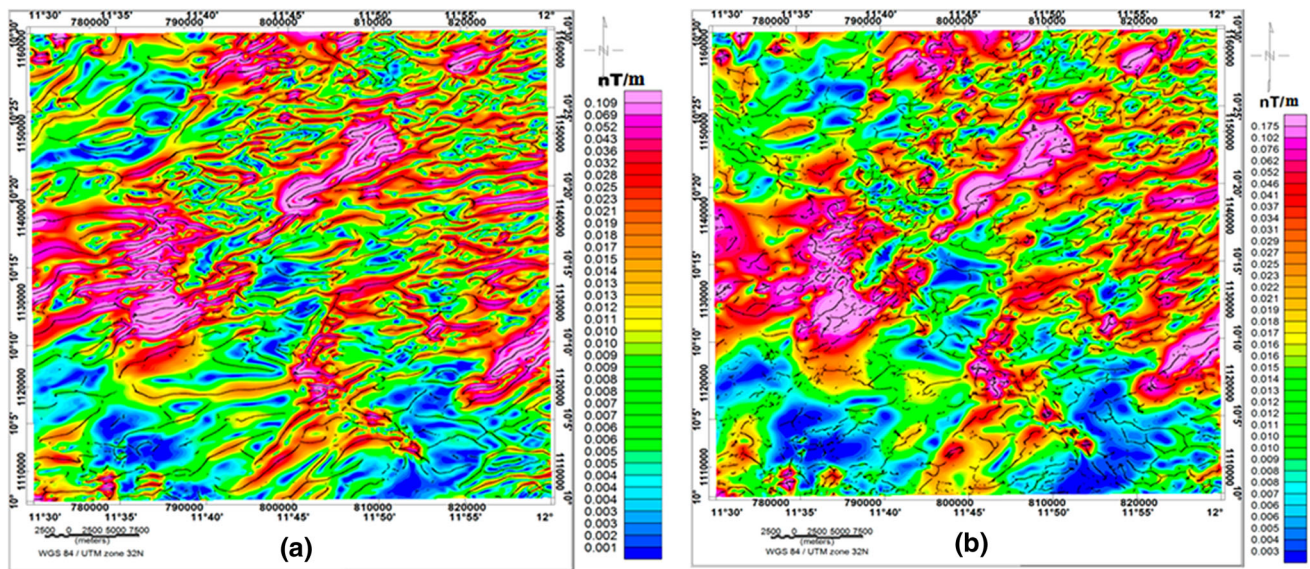
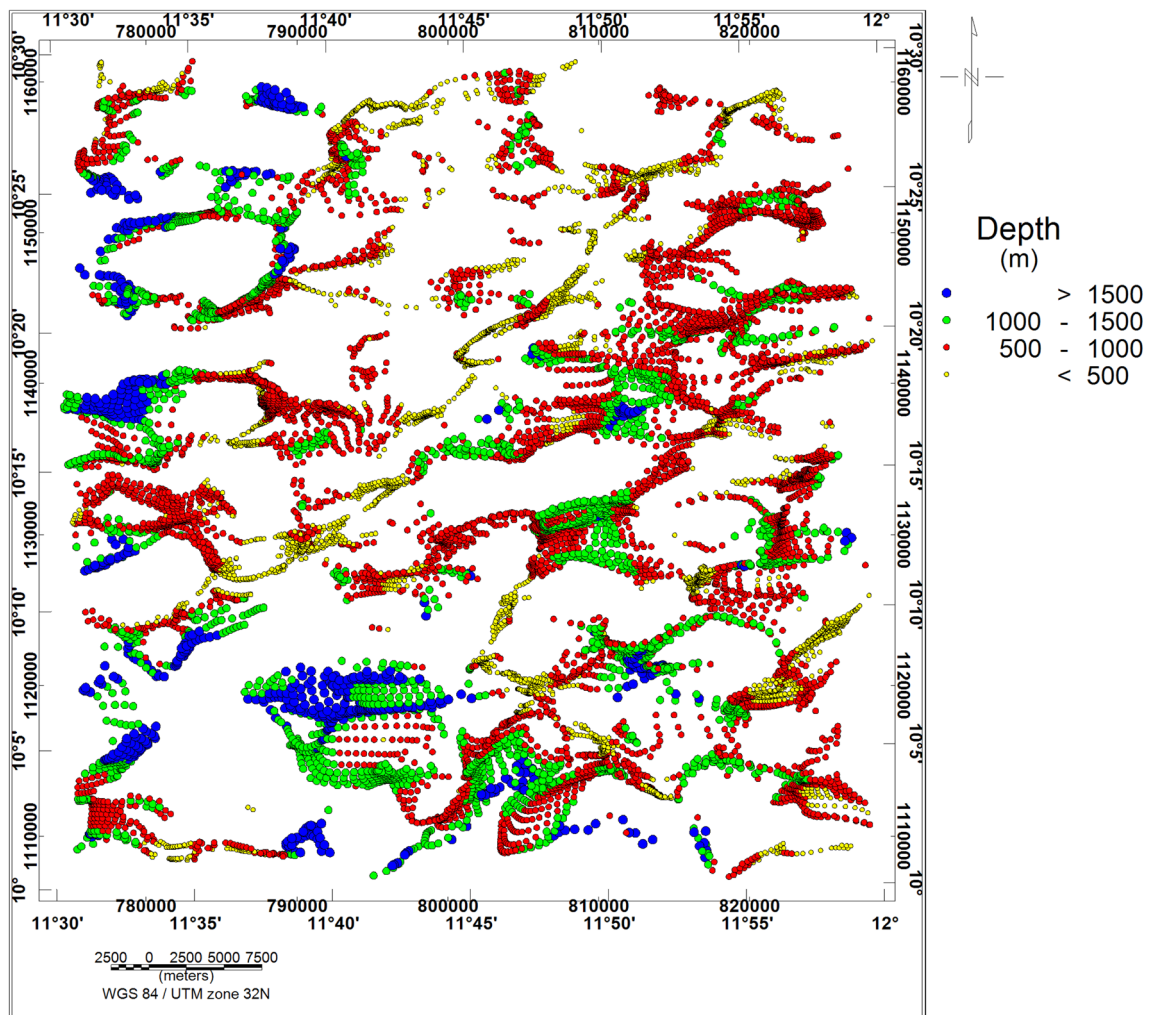Fig. 7 a Peaks overlain on the HGM map; b peaks overlain on the AS map

Fig. 8 Euler solution map for a structural index (N) of 1

terrain of the study area. These structures could be faults on or within the basement.

Composite map

The composite map (Fig. 9) was produced from the superposition of HGM maxima (red), ASA peaks (pink), ED solutions (yellow), and the First vertical Derivative (FVD) image of the filtered RTE map. The FVD image forms the background, while other maps were overlain. The integration of several methods for detecting source edges served as a reliable factor of confidence in mapping the geological structures. Superposition of HGM maxima and AS peaks helped in determining the actual location and the dip direction of the structures. According to Philips (2000) and Ndougsa-Mbarga et al. (2012), AS contact map shows the true contact location, while areas where the

HGM contacts are slightly parallel or offset from analytical signal located contacts signify the down-dip direction; however, when both overlay each other, the contact is said to be purely vertically dipping. The ED solutions obtained from using structural index of one were used to differentiate possible fault locations from lithological contacts. The FVD of the magnetic anomalies was carried out to sharpen the locations of the structures, and also aid in tracing other contact locations, extensions, and continuation that were not fully detected by the HGM and AS.

Inferred structural map of the study area

The structures delineated from the composite map were compiled to produce the structural map for the study area (Fig. 10). The structural map generally illustrates that the basement rocks are bounded by many contacts and faults
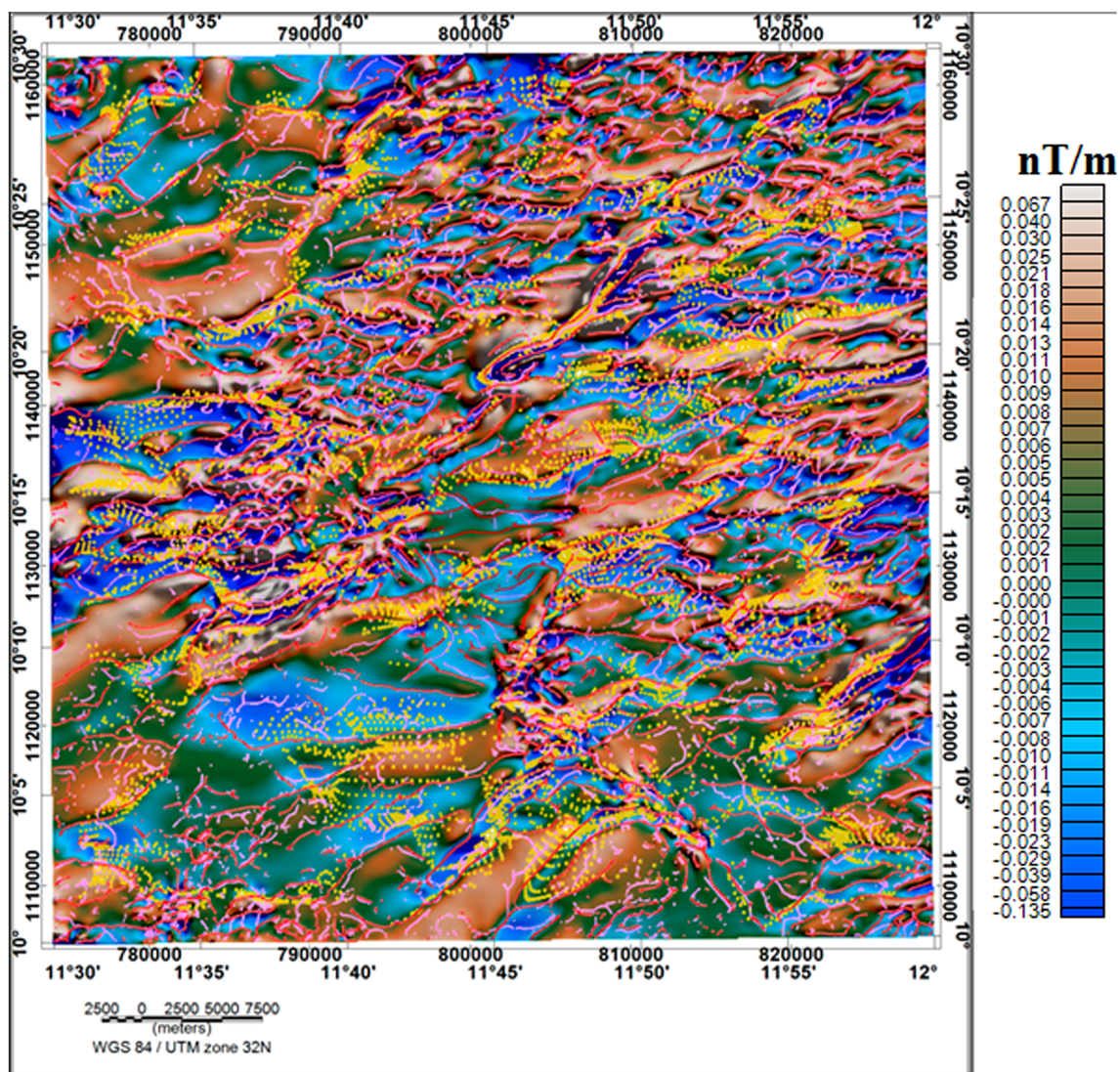

Fig. 9 Composite map of the estimated contact locations from HGM (*red*), AS (*pink*), and ED (*yellow*) overlain on FVD of the RTE map

that trend and dip in various directions. The black and red lines in the map, respectively, depict the inferred contact and fault locations. The short lines perpendicular to the strikes of the inferred faults indicate the dip directions. The faults without dip direction are considered vertical. The geological structures in the study area trend in the ENE–WSW, NE–SW, E–W, WNW–ESE, and NW–SE directions. These structures are more concentrated in the basement complex part of the study area than the sedimentary terrain. This is as a result of the closeness of the basement to the surface; the magnetic contours in cretaceous rocks are normally smooth with small variations which reflect the

basement rocks than the near surface features, while igneous and metamorphic rocks dominated areas normally exhibit complex magnetic variation (Telford et al. 1990).

The orientations (azimuth directions) of the lineaments on the structural map were measured and plotted on a rose diagram. The azimuth-frequency (rose) diagram (Fig. 11) shows that the geological structures in the study area majorly trend in the ENE–WSW and NE–SW directions. Few azimuthal frequencies were recorded for structural lineaments that trend in the E–W, NNE–SSW, WNW–ESE, and NW–SE directions. The NNE–SSW/N–S trends, which are very prominent Northeastern Nigeria, are related
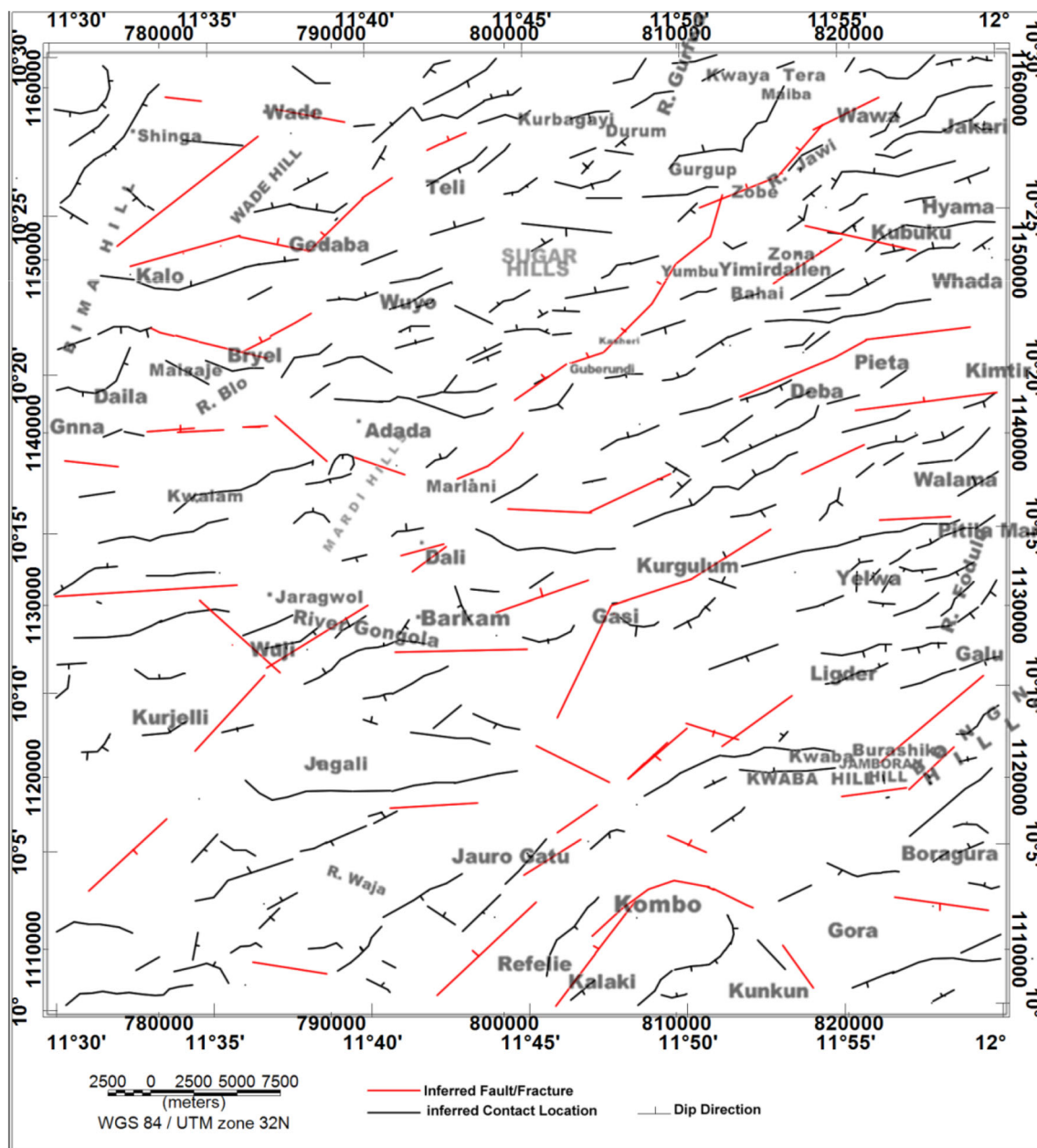

Fig. 10 Inferred structural map of the study area

to the late reactivation of Pan-African basement complex (Suh et al. 1998), while the E–W trends according Obiora (2009) are said to be pre-Pan African (over 800 Ma). The dip direction, as observed on the structural map, varies for different lithological contacts with dominant ones dipping in the NNW, SSE, NW, and SE directions, while others dip vertically, northeasterly, or southwesterly.

Radiometric interpretation

Equivalent Thorium (eTh) surface distribution map

Figure 12 shows the eTh distribution map of the study area overlain by the geological map. The geological map was superimposed to relate the observed eTh concentration with geology of the study area. The eTh distribution map has eTh concentration ranging from 6.67 to 47.85 ppm. For the purpose of this interpretation, the eTh concentration in the study area will be relatively grouped as high (>29 ppm), moderately high (21–29 ppm), moderately low (14–21 ppm), and low (<14 ppm).

The superposition of the geological map on the eTh surface distribution map has shown the significant relevance of radiometric data in geological mapping. The Bima sandstones at the northwestern flank of the study area are characterized by low eTh concentration, while moderately low-to-moderately high concentrations were observed at the neighbouring Pindiga formation. The sediments in the western and southern regions generally give low-to-moderately low eTh signature; these regions span the Bima, Yolde, Pindiga, and Jessu formations. The granitic rocks, forming the basement complex terrain of the study area, generally show strong signatures of thorium concentration. The NE–SW and E–W trending anomalous zones of high eTh content in the northern region are dominated by coarse porphyritic granite, biotite/muscovite granite, and anatectic migmatite, whereas the nearby Yolde, Pindiga, and Bima formations show relatively low concentration. In addition, the granitic rock in the northwestern region gives a distinct high thorium count from the bounding sediments of Pindiga, Yolde, and Bima formations which show low-to-moderately high eTh concentrations. The nearly circular high eTh concentration anomaly observed in the western

Fig. 11 Azimuth-frequency (rose) diagram of the inferred structural contact location

Fig. 12 Superposition of geological map on eTh concentration map
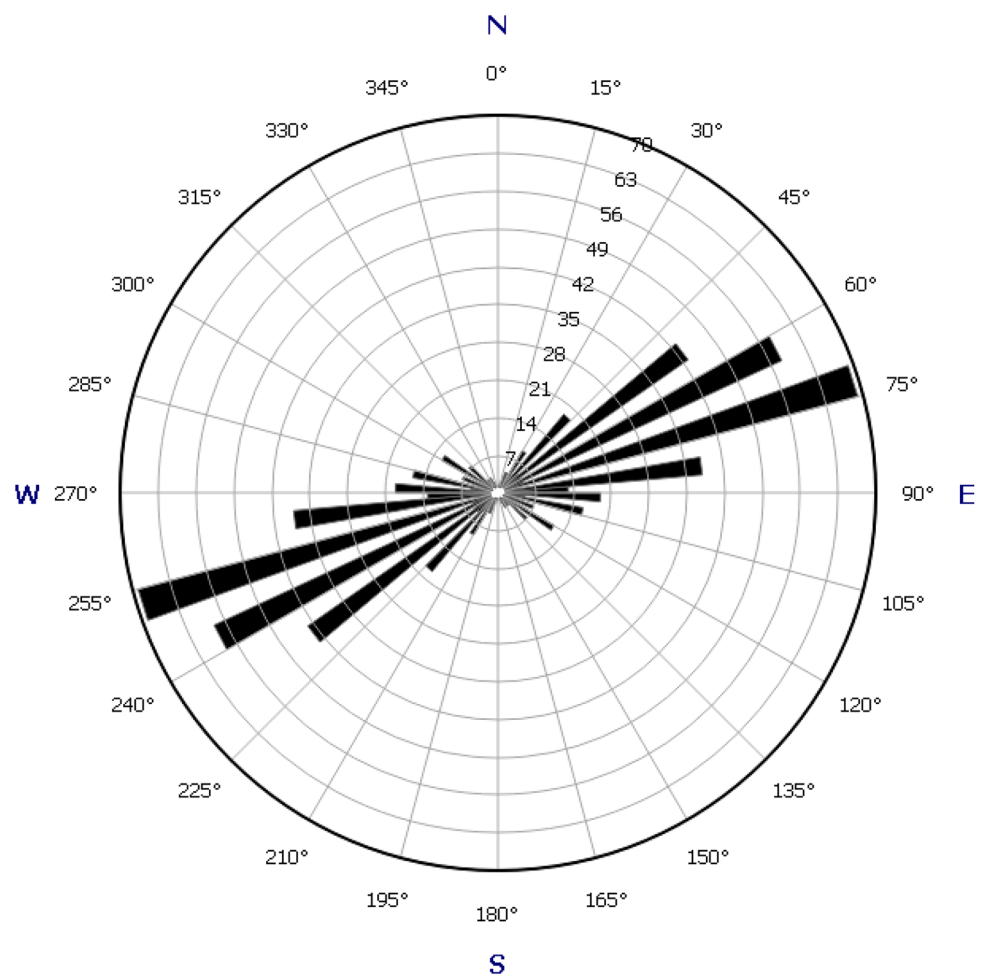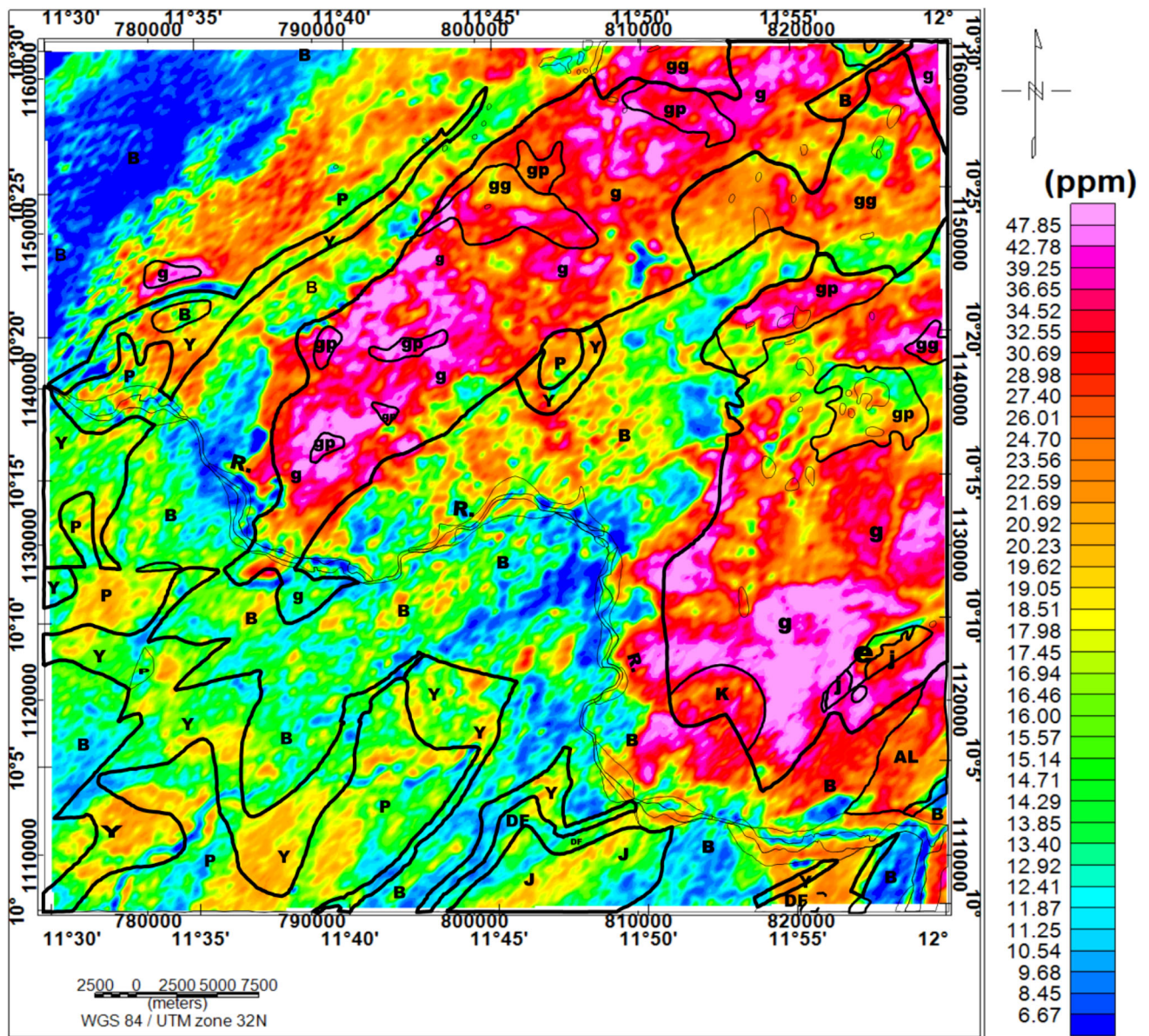
AL — Alluvium

J — Jessu Formation

DF — Dukul Formation

P — Pindiga Formation

Y — Yolde Formation

B — Bima Sandstone

e — Bongna Hills lavas and agglomerate

j — Jamboram Hill porphyry

R. — River Gongola

K — Kwaba Hill granite

gP — Coarse porphyritic granite

g — Biotite/Muscovite Granite

gg — Anatectic migmatite

and southeastern regions is also dominated by granitic rocks. The Jamboram and Kwaba hills have moderately high-to-high concentrations, while the major part of the Bongna hill shows relatively low eTh concentration. Low eTh counts were recorded in most parts of the riverine areas.

Equivalent Uranium (eU) surface distribution map

In radiometrics, estimates of uranium concentration are usually reported as equivalent uranium, because these estimates are always based on the assumption of equilibrium conditions. Figure 13 shows the eU concentration map and geological map of the study area superimposed. The map shows various anomalous signatures with total eU concentrations varying between 0.5 and 6.8 ppm. The eU concentrations can be relatively grouped as high (>4.63), moderately high (3.66–4.63), moderately low (2.64–3.66), and low (<2.64). Most of the granitic bodies in the study area are associated with high eU signature, while the outer zone of the granitic rocks displays moderately low-to-moderately high counts. The anatectic-migmatite inlier which was intruded by the granitic rocks also has high uranium concentration. The Bima formation at the extreme of the northwestern flank of the study area shows a characteristic of low uranium concentration; however, very few intercalations of high signatures were recorded within it. The biotite/muscovite granitic inlier in this area also shows high uranium concentration. The Bima sandstone between the Yolde formation and the granitic body in the northwestern region gives relatively moderate-to-high count, while the Pindiga formation and the Yolde formation show low-to-high uranium concentration. From the western region down to the southern region, the Bima, Yolde, Jessu, Dukul, and Pindiga Formations are characterized by moderately low-to-moderately high uranium concentration.

As observed on the eTh and eU concentration maps, the river channel in the study area gives low values for eU and eTh concentrations. However, this does not mean that it does not contain radioactive material, but it is as a result of water being a strong absorber of radiation (Darnley 1975).

Ratio maps

Ratio maps are maps generated from meaningful arithmetical combination of two radioelement grids. These maps assist in the reduction of the effects of environmental factors (such as vegetation, soil moisture, topography, and weather condition) on the recorded radiometric data. In this study, three ratio maps [eU^2/eTh, eU/eTh, and $eU–(eTh/3.5)$] were adopted.
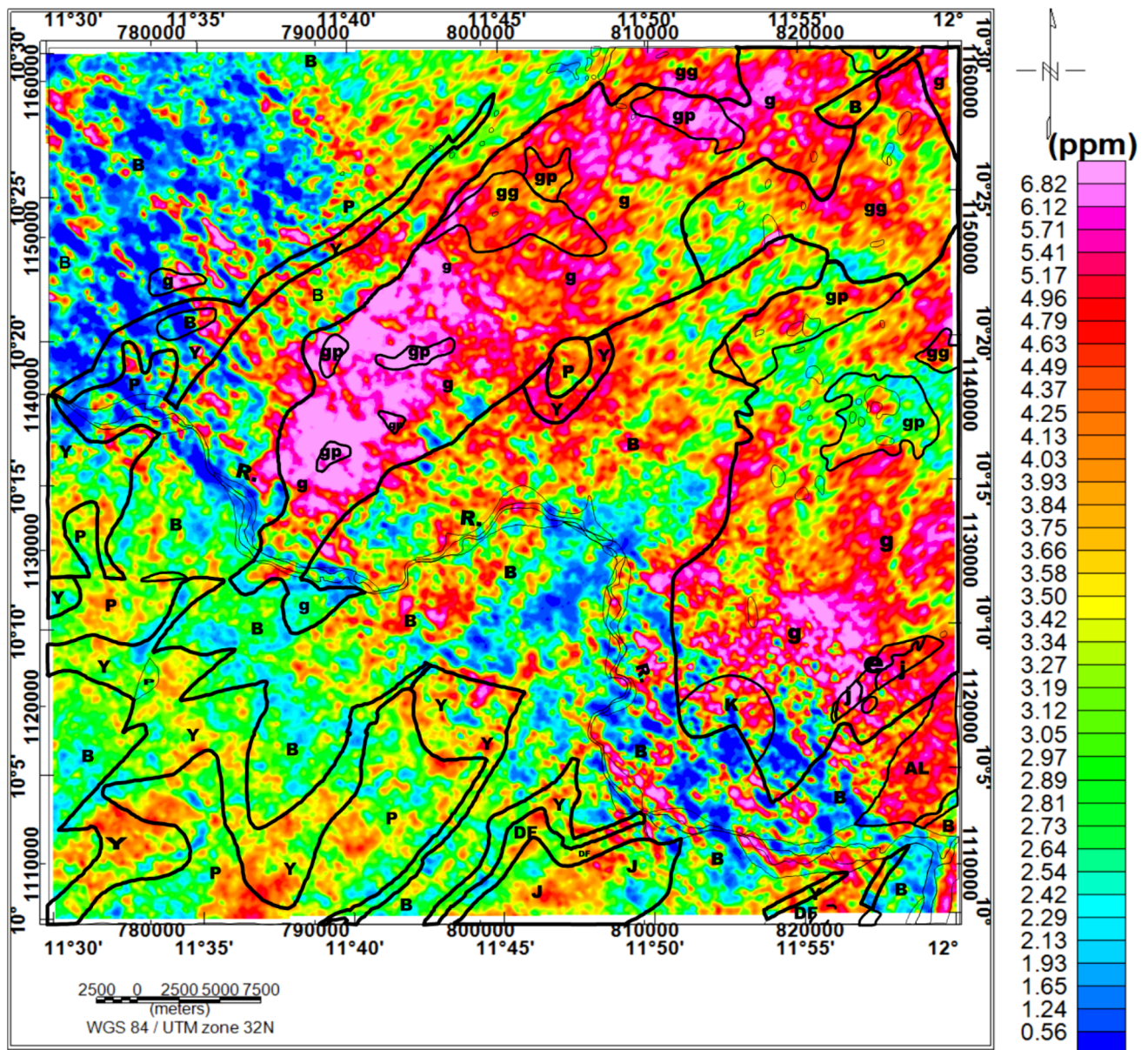
eU^2/eTh Map

The eU^2/eTh map was obtained by squaring the eU map and then dividing the resulted map by eTh map. The eU^2/eTh ratio map assists in the amplification of areas with high eU concentration which was decreased by damping effect of media (e.g., water). This ratio map transforms the eU measurement towards the ideal case in which the bedrock is not covered by soil or water (Lauri and Turunen 2015).

The eU^2/eTh map of the study area is presented in Fig. 14. On this map, various anomalous zones which were not shown in the eU concentration map were observed; however, some high counts in the eU concentration map were also suppressed. The values of the eU^2/eTh map range between 0.042 and 1.65 ppm. The granitic bodies in the study area still show high values, though less prominent than on the eU concentration maps. However, the Bima formations in various parts of the study area show more concentration than those on eU map. The Bongna hills lava and agglomerate at southeastern region still retain their high concentration. The formations at western, southwestern, and southern flank of the study area also retain their moderate concentration. The alluvial deposits at the southeastern part of the study area show significant eU concentration.
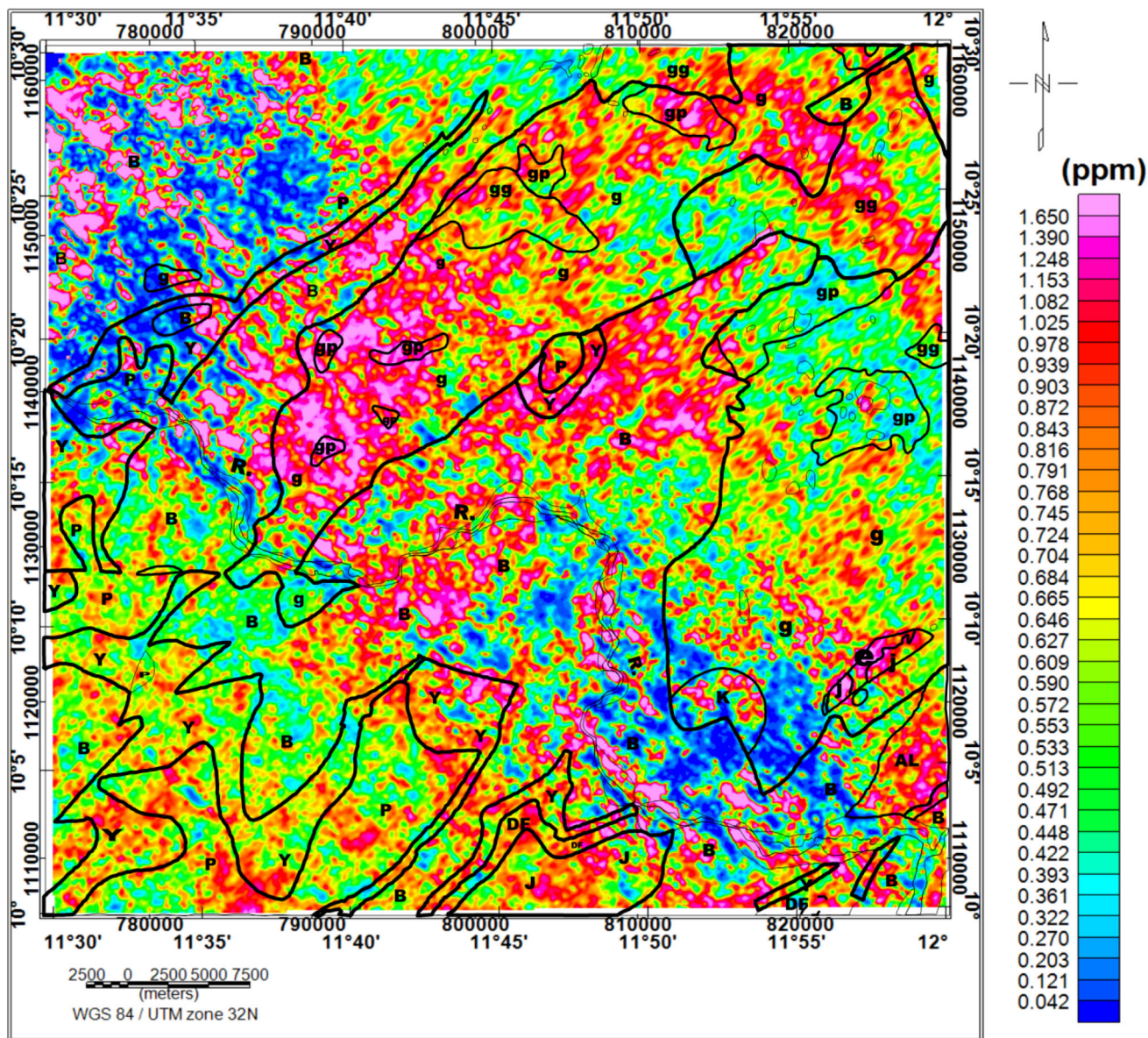
eU/eTh map

The eU/eTh ratio, which is important in uranium exploration, depends mainly on the mobile elements (i.e., uranium), and it also determines uranium enrichment areas (Gaafar and Aboelkhair 2014). According to Clark et al. (1966), the eU/eTh ratio for granitic rock is about 0.33; the enrichment area is above 0.33 in granites, while leaching out of uranium will be indicated by its decrease to less than 0.3 (Gaafar and Aboelkhair 2014). From the eU/eTh ratio map (Fig. 15), most of the granitic rocks in the study area have relatively low values compared to the surrounding lithological formations such as Bima, Yolde, and Pindiga. This shows that the granitic bodies in the study area are likely to be richer in thorium than uranium, and in addition, the ratio values suggest that uranium is leaching out from these bodies. In the northern part of the study area, the Bima formations at the opposite sides of the NE–SW trending granitic body show very high (>0.33) eU/eTh ratio. This shows that uranium ore is likely to have been deposited in the Bima sandstones. The Bongna hill also shows high ratios, while the Pindiga, Yolde, Bima, Dukul, and Jessu formations located at the western, southwestern, and some parts of the southeastern portions of the study area show intercalations of eU/eTh ratio anomalies ranging from moderate to high. It was also observed on the eU/eTh map that some parts of the Bima formation close to the
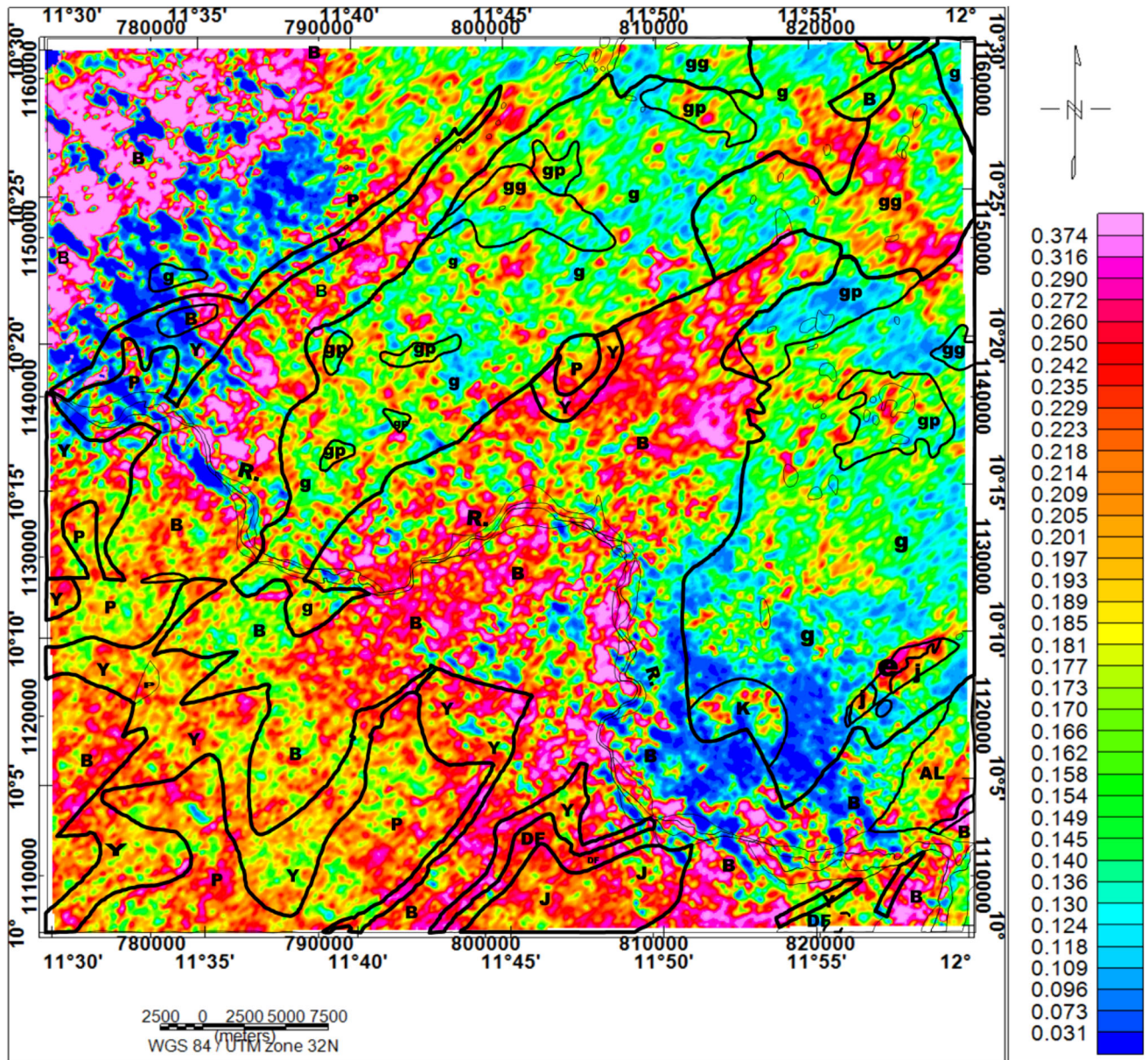
Fig. 13 Superposition of geological map on eU concentration map

Fig. 14 Superposition of geological map on eU^2/eTh concentration map

Fig. 15 Superposition of geological map on eU/eTh concentration map

riverine areas at the southeastern flank of the study area show high ratio. The uranium enrichment of the sandstone (Bima sandstone) might have resulted from the precipitation of soluble uranium deposits flowing along the river channel.

eU–(eTh/3.5) map

Uranium is a mobile element which can be liberated from the source, transported in aqueous solutions and deposited in various environments due to redox changes, absorption, precipitation, or metasomatism or due to a combination of some of these processes (Ruzicka 1975). This kind of deposition occurs under various pressure and temperature (P–T) conditions. Uranium redistribution or remobilization in this area can be estimated by dividing the eTh content by 3.5 (the eTh/eU ratio in granitic rocks) and subtracting the result from the eU content (Clark et al. 1966; Cambon 1994; Gaafar and Aboelkhair 2014). The resulting map, which is useful in defining the trends of uranium migration, shows the hypothetical uranium distribution; the negative contour areas connote the leaching area, while the positive, deposition (Gaafar and Aboelkhair 2014). The direction of the uranium mobilization can be traced with directions trending from the negative anomalies to the high positive ones (Gaafar and Aboelkhair 2014).

Figure 16 shows the eU–(eTh/3.5) distribution map of the study area. The labels A, B, C, and F on the distribution map are uranium rich Bima formations, while D and E are the migmatite and Bongna hill uranium rich rocks. Directional arrows D1, D2, D3, and D4 show the hypothetical directions from leaching to deposition. D1 shows the direction arrow for leaching uranium from the NE–SW trending granitic rock into B and C. Also from the map, direction D2 shows that the granitic rock in the northwestern part of study area is leaching, and it is being deposited into A. The continued leaching of the NE–SW trending granitic body through B might have also contributed to the uranium deposition in A. The granitic rock spanning the eastern and the upper part of the southeastern region is leaching in various directions (D3, D4, D5, and D6). D3 shows that the uranium particles leaching out from the granitic rock have also contributed to the deposits in C. D4 and D5 show the directions of uranium leaching from the granitic rock into F and other formations in the lower part of the southwestern region. Zone D in the northeastern part of the study area shows the likelihood of uranium rich basement rock, whose surrounding rock is leaching out. The eU–(eTh/3.5) map of the study area has prominently shown that the uranium ore leaching from the granitic rocks is mostly deposited in the Bima formations, and these deposits (A, B, C, F, and E) trend in the NE–SW direction, while D trends in the NW–SE direction.

Superposition of the inferred structural map on eU/eTh map

The superposition of the inferred structural map on eU/eTh map assists in delineating structural features that are rich in uranium. The superposition map for the study area is presented in Fig. 17. The high eU/eTh ratio areas in this study were grouped into eight zones, which were labelled: J, K, L M, N, O, P, and Q. The possible areas of uranium deposition indicated on the eU – (eTh/3.5) distribution map (Fig. 16) were also taken into account when marking the uranium-enriched zones (i.e., zones J–Q) in the study area. It was observed on the map that the zones consist of many structural features that are dominantly trending in the NE–SW directions. Among these structural features are inferred faults, also dominantly trending in the NE–SW direction. Zone J, comprising Wade and Shinga districts, is dominated by NE–SW trending structural features. Other notable structures in the zone trend in the NW–SE and E–W directions. Three structure spanning several kilometres were prominent in this zone. One of these structures is a fault that has a high potential of hosting uranium deposits in its vein.

Majority of the structural trends at Zone K, consisting of Wuyo, Teli, Gedaba, and Bryel town, are in NE–SW direction; however, two structural faults trending in the NW–SE and E–W directions are also present. Zone M, whose deposition trends in the NW–SE direction (Fig. 17), comprises Gasi, Dali, and Barkan settlement; this zone contains majorly NE–SW structural features, but minor NW–SE structural features also exist. Zone N covers Boragara settlement; this area also comprises some alluvium deposits that are rich in uranium with faulted zone trending in E–W direction, while other structural features in the area trend in NW–SE direction. Zone L, comprising Zona, Yumbu, Yimirdallen, and Bahai settlements, has been reported by several authors (Suh et al. 1998; Oshin and Rahaman 1986) to be rich in uranium. Most structures in the zone trend in the NE–SW direction, except one, which trends in the NW–SE direction. Zones O and P, which are from the Burashika group, are made up of diverse suite of extrusive lavas and agglomerate to form the Bongna hills. These zones are characterized by two structures, a fault and contact zone, trending in NE–SW; these fault and contact zones are likely to contain high uranium deposits. Zone Q, which trends in the NW–SE direction and covers Whada, Wawa, Jakari, Hyama, and Kubuku settlements, is also dominated by NW–SE and NE–SW structural features; however, some NE–SW features also exist in the area.

From the map (Fig. 17), it was observed that the dominant structures that are rich in uranium trend in NE–SW direction, while the directions of leaching (Fig. 16), which
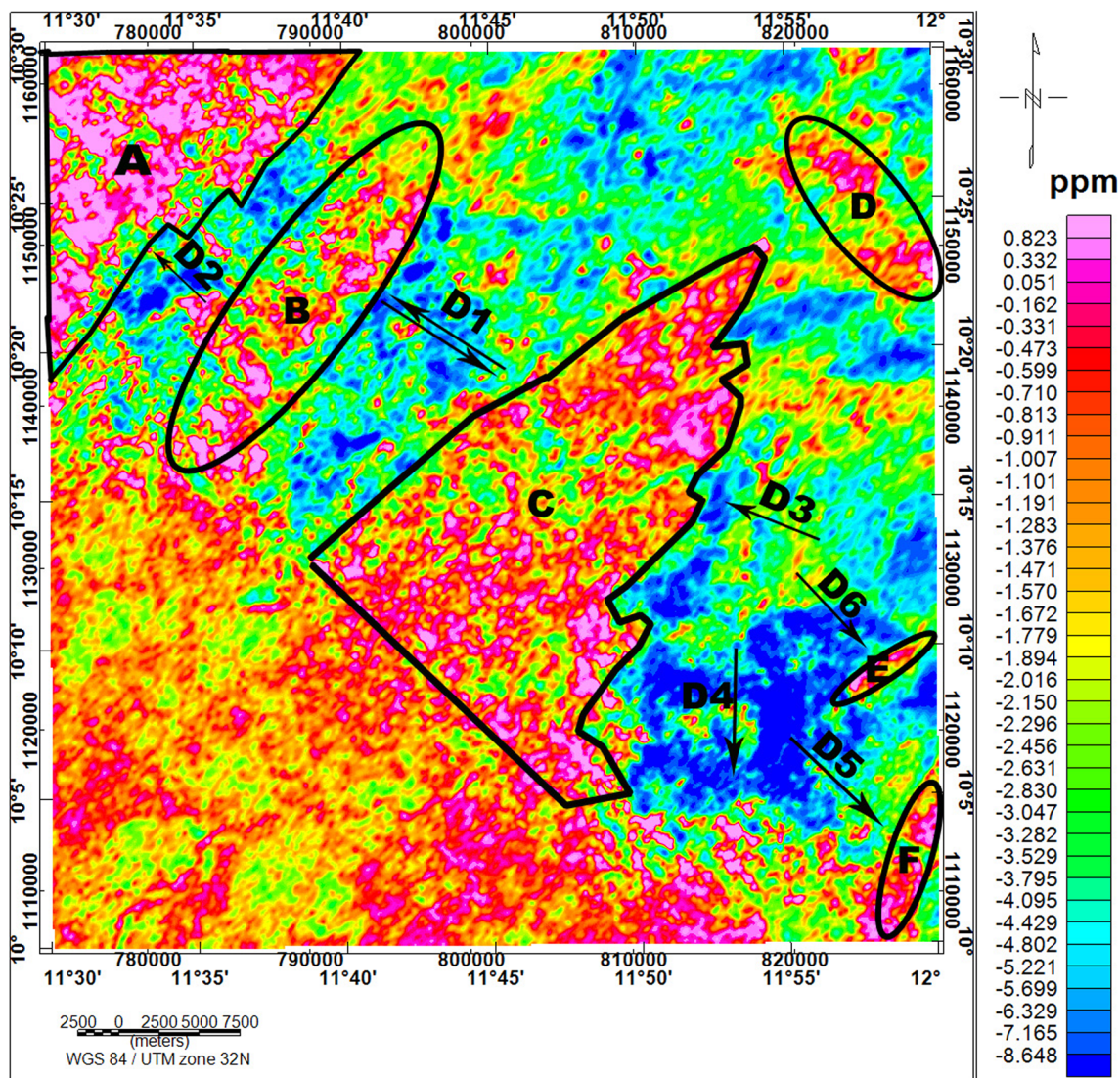
Fig. 16 eU–(eTh/3.5) map with the directional *arrows* showing the hypothetical trend of uranium migration

is also the paleocurrent direction for sediments in the area according to Haruna et al. (2012), are towards NW and SE. The perpendicular nature of the structural feature to the leaching direction has made this dominant structural trend to be more favourable for uranium deposition. Some of the NW–SE trending structures in the study area have been reported by Suh et al. (1998) to be rich in uranium.

Magnetic modelling of some selected uranium rich areas

Magnetic modelling of two profiles taken across some uranium rich zones (Fig. 18a) were carried out to provide 2D images of the subsurface that more accurately represent the topography, magnetic property, and structural geometry of the basement along the profiles. The profiles, labelled PP′ and TT′ in Fig. 18b, were taken in the NW–SE

direction. The result of the SPI analysis (Fig. 6) was used as depth constraint, and the resulting models along these profiles, PP′ and TT′, are presented in Fig. 18c, d.

As shown in Fig. 18c, d, profiles PP′ and TT′ were modelled as 29 basement blocks (R1–R29) and 21 basement blocks (R1–R21), respectively. The magnetic susceptibilities of the modelled blocks range from ∼0.0001 to ∼0.007 and ∼0.002 to ∼0.005 cgs across both profiles. The high number of visible basement blocks was as a result of the high-resolution aeromagnetic data used. Most of the contacts (boundaries) between these magnetic blocks were modelled to be approximately vertically dipping.

On PP′ profile, contacts between blocks R15 and R16, and blocks R25 and R26 show magnetic anomaly that is more typical of a fault. Variation in the basement topography was also observed, with the sedimentary thicknesses of the entire area undulating between 35 and 1125 m on the
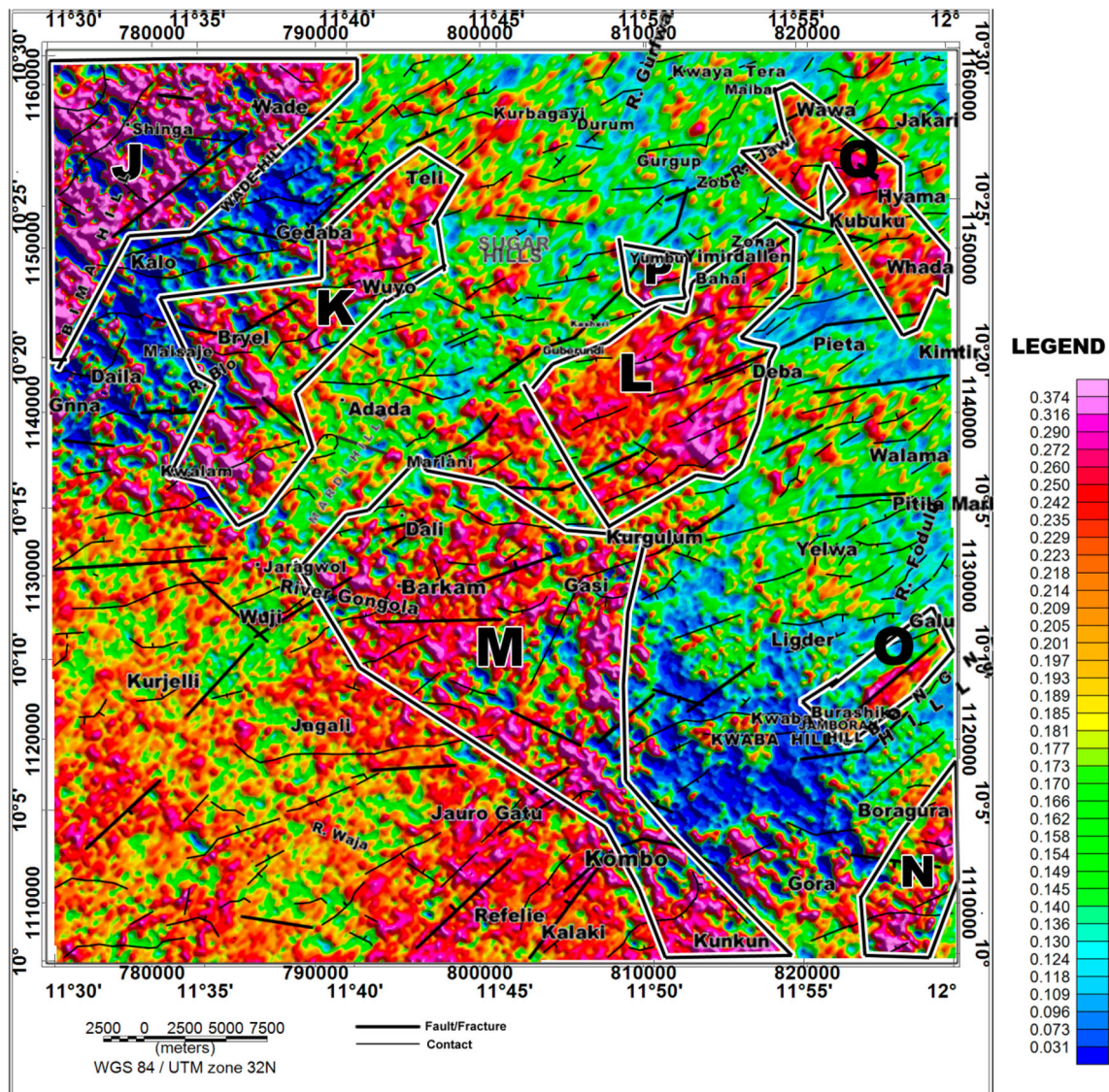
Fig. 17 Superposition of inferred structural map on eU/eTh map with selected zones with high concentration

magnetic basement. The uranium rich areas on the profile were labelled A, B, C, and D. At D, the interpreted fault between R25 and R26 is characterized by high uranium concentration on the eU/eTh ratio map (Fig. 15) and the eU–(eTh/3.5) distribution map (Fig. 16). This fault is, therefore, likely to be vein hosting uranium deposits. The areas marked B and C have relatively thick overburden with magnetic basement having susceptibilities ranging between ~0.004 and ~0.007 cgs. However, the basement rock below A is characterized by lower susceptibility of ~0.001 cgs. Each of these observed points (B, C, and D) shows a basin basement structure that is bounded on both sides by ridges. These ridges are likely to be the sources of the sediments deposited in this basin like structure.

On TT′ map, the uranium enrichment area covers blocks R7–R19. The modelled overburden thicknesses of this area

range between 13 m and 749 m. Contact between blocks R6 and R7 shows the magnetic signature of a geological structure which is likely to be a dyke or vein. The inferred structural map (Fig. 10) also shows that the location of this contact is a faulted zone. The trend of the contact is perpendicular to the trend of the high eU/eTh ratio anomaly observed in the region. This structure is, therefore, likely to contain uranium ore deposits.

Discussion

The study area, being a transitional zone, encompasses both the basement complex and sedimentary terrain. The result from the eU and eTh maps shows that the granitic bodies in the study area are rich in uranium and thorium

Fig. 18 a Profiles taken across
the uranium rich zones.
b Profiles' locations on filtered
RTE map. c Magnetic model
along profile P–P′. d Magnetic
model along profile T–T′

(a)

(b)
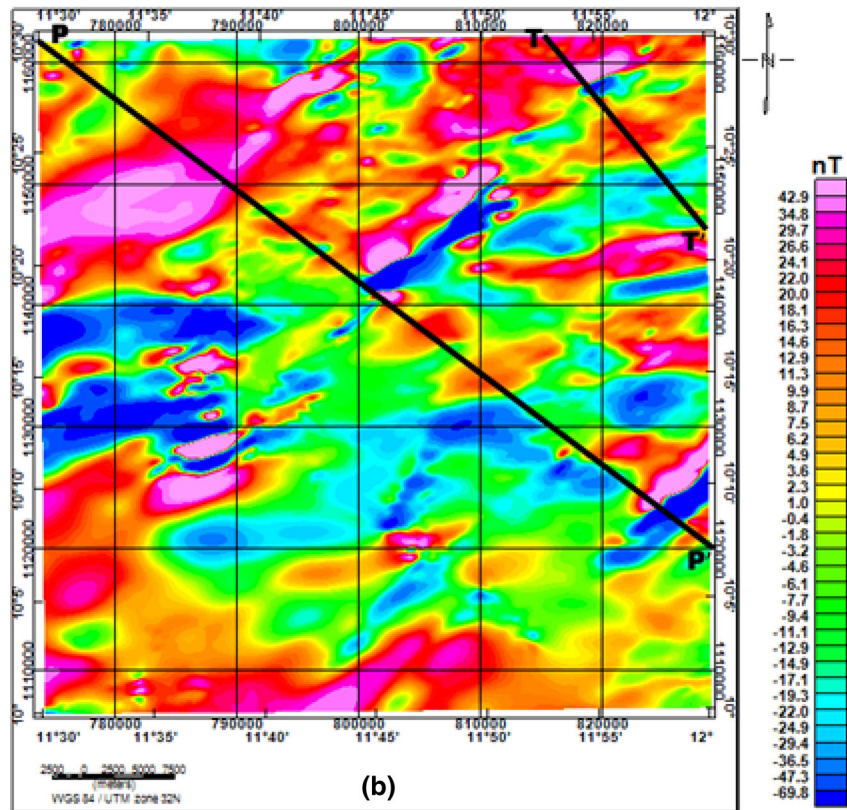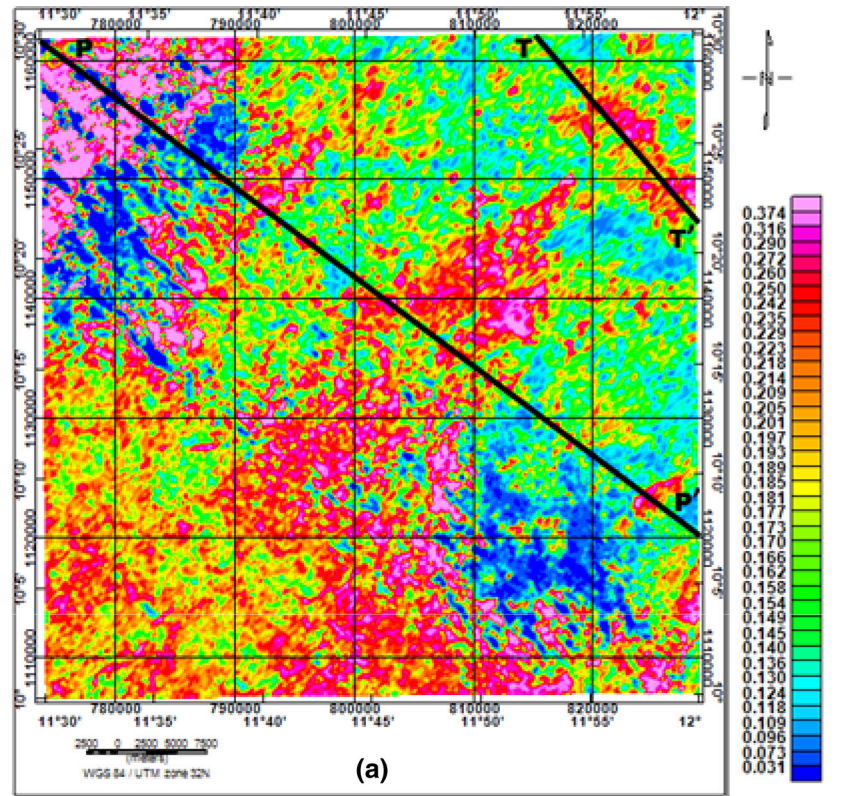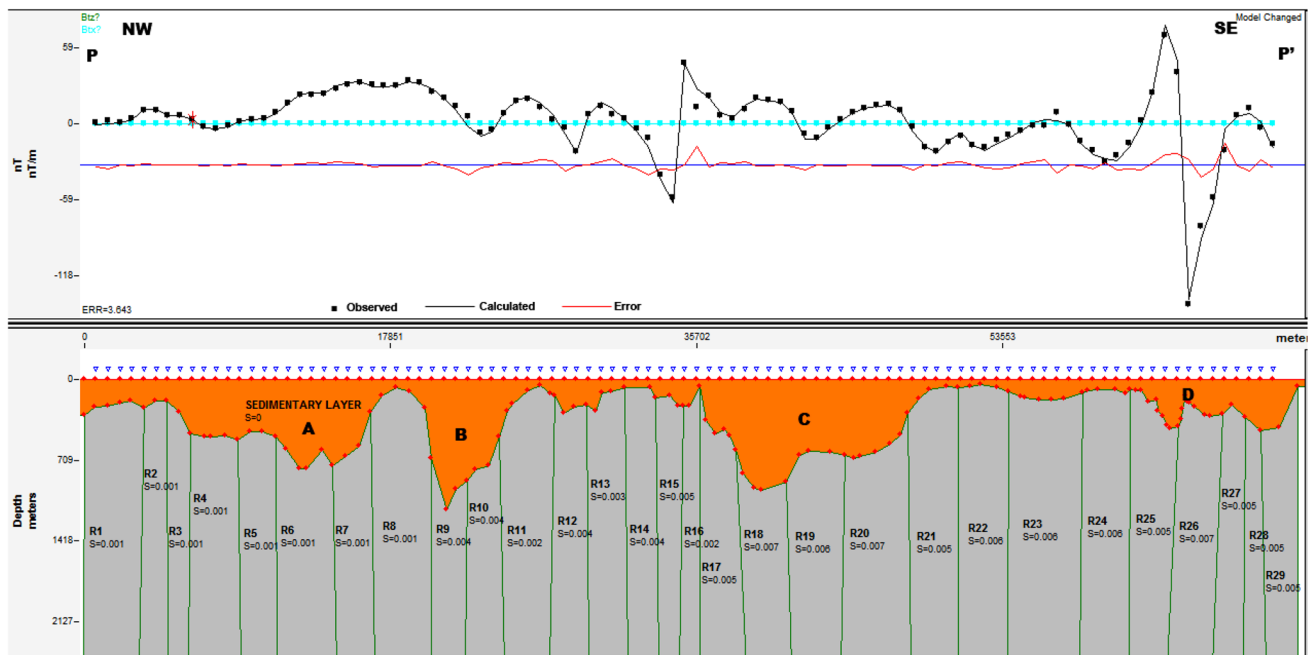
(c)

(d)

Fig. 18 continued

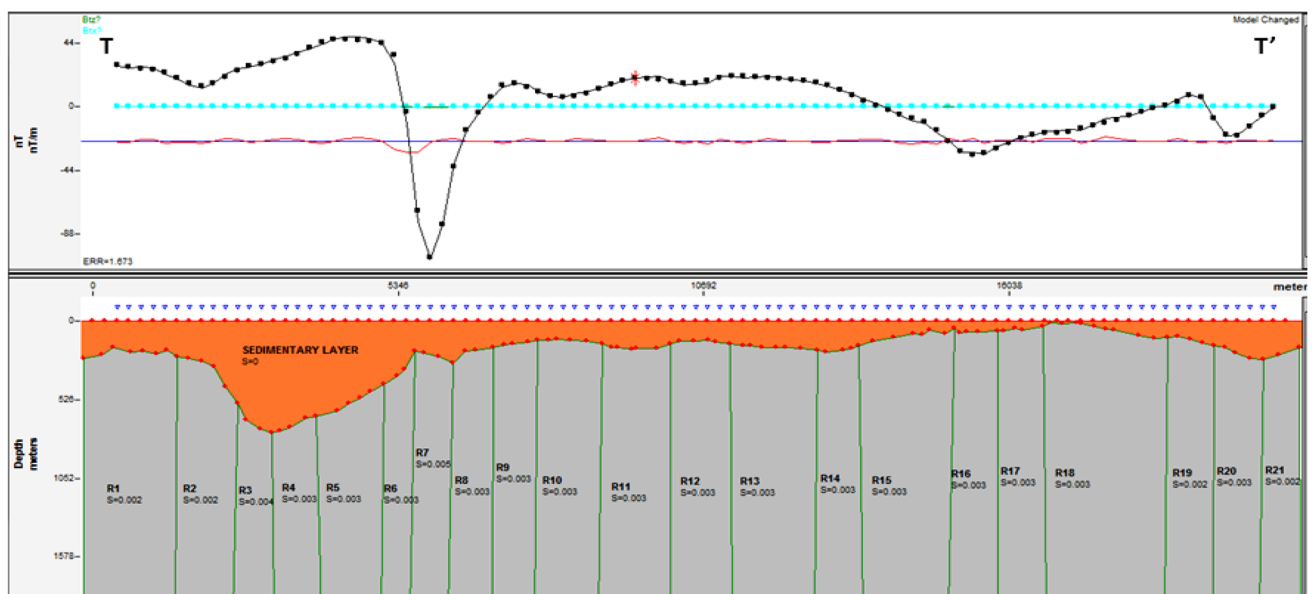than cretaceous rocks in the area. However, uranium which is the major interest in this study cannot be single handedly interpreted based on eU and eTh maps, because the source geometry clearly affects the absolute count rate, but has no effect on relative count rates; therefore, the use of ratio maps showing relative count rates was employed. The eU^2/eTh map reveals other uranium enrichment areas that were not exposed by the eU map which may be as a result of vegetation or damping effect. On the eU^2/eTh map, granitic

bodies, the Bima formation, and some other alluvium deposits were revealed. However, the eU^2/eTh map did not reveal areas suitable for uranium exploration, and this led to the use of eU/eTh ratio map which shows more defined uranium enrichment area. The eU/eTh map reveals that the granitic bodies are not extremely rich in uranium compared to Bima formation, Bongna hill lavas and agglomerate, and the anatectic migmatite at the northeastern region of the study area. The Burashika group (Bongna hill) at the

southeastern flank, anatectic migmatite at the northeastern region and most of the Bima formations in the study area show high eU/eTh concentration ratio of about 0.374. However, other sedimentary formations such as Yolde, Pindiga, Jessu, Dukul, and even the Bima formation at the southwestern region of the study area show moderate uranium concentration. These formations (Yolde, Pindiga, Jessu, and Dukul) are, therefore, not geologically ascertained for uranium deposition.

The possible trends of uranium distribution in the study area were shown on the $eU - (eTh/3.5)$ map (Fig. 16). The map hypothetically reveals the leaching rocks and the direction of remobilization of uranium ore, with its source shown to be from the granitic bodies in the study area. The deposition observed in the region according to the $eU - (eTh/3.5)$ map is secondary deposition (epigenetical remobilization of uranium ore). In addition to what was observed in the $eU - (eTh/3.5)$ map, the result from magnetic basement depth analysis using SPI and forward modelling techniques shows basement highs at both sides of the uranium rich formations, while the locations of these uranium rich formations show pull-apart sub-basin structures. The basement morphological map, obtained from the radially averaged power spectral, shows horst and graben structures in the basement complex and sedimentary terrain, respectively.

The Bima (sandstone) formation was observed as the uranium richest sedimentary formation in the study area. This sandstone formation (Bima), being the most outcropping formation of the Upper Benue (Suh et al. 1998), has been reported by Carter et al. (1963) and Guiraud (1990) to contain three (3) lithological units known as lower Bima (B_1), middle Bima (B_2), and upper Bima (B_3). B_1, representing alluvium fan deposit, contains coarse-grained sandstone with matrix of scanty-muddy-to-sandy matrix; B_2, whose deposits were from high braided river deposits, comprises coarse-grained feldspathic sandstone with thin bands of clay, shale, and scanty calcareous sandstone, while B_3, whose sequence deposited under fluviatile to deltaic environment, consists of well-sorted, medium-to-fine-grained feldspathic sandstone. Furthermore, the loose cementation and fine-to-medium-grained properties of Bima formation enabled the permeability of the uranium rich groundwater (since uranium is soluble in water) into the formation, and the calcareous (organic debris of animals) sandstones present in this formation served as the reducing agent for the precipitation of uranium. This type of deposition is also found in Canada (British Columbia), Western United States (Jack Pile mine, Lucky Mack mine), East Germany (Koenigstein), Gabon, Niger Republic, and South Africa (Karoo Basin) (Bell 1996; Ruzicka 1975, 1992). However, this region, which has been subjected to regional uplift and effects from various volcanic activities, also

shows likely abundant tectonic traps for deposition of uranium ore. It is a known fact that geological structures play a vital role in the formation, migration, and deposition of minerals in an area. The results from the structural mapping of the study area show that the basement in the study area is dissected, at various depths, by many structures that trend and dip in various directions. The dominant trends of the structures are ENE–WSW and NE–SW, while the minor structural trends are E–W, NNE–SSW, WNW–ESE, and NW–SE. The structures dip vertically, northeasterly, southwesterly, northwesterly, and southeasterly. The major ones, which dip northwesterly and southeasterly, trail in the same direction as the paleocurrent directions (Haruna et al. 2012), which is the direction of depositions of sediments in the study area. The basement faults in the study area dominantly exist between the depths of 500 and 1000 m. The NE–SW trending faults, which could have been created or reactivated during the reactivation of the Pan African basement, are perpendicular to the direction of uranium deposition in the study area and thus could have served as a trap for the migrating uranium. These NE–SW structural features show the highest uranium rich structural trends and were observed in both the sedimentary and basement complex uranium rich terrains. Uranium deposition in the sedimentary terrain of the study area is likely to be a sandstone type of deposition, while uranium depositions in the faults/fracture veins of the basement complex terrain might have also been formed as a result of the occurrence of volcanic activities in the area. These volcanic activities might not only have provided the thermal energy fluid containing dissolved uranium ore, but might have also served as a reducing agent for the precipitation of uranium ore.

The HRAD and radiometric data analyses, and the geological settings of the study area show that the Bima sandstone formation serves as a reservoir for uranium mineralization bearing solutions. The fault, fracture, and contact zones in the sedimentary units show the tendency of providing favourable post depositional zones for uranium concentration. Wade, Zona, Shinga, Bima Hill, Wuyo, Teli, Bryel, Dali, Barkan, Gasi, Kunkun, Boragara, and Deba localities have shown high affinity for uranium depositions in the sedimentary unit of the study area. Whada, Gberundi, and Kubuku localities in the basement complex unit also show high affinity with uranium depositions. In addition, the Burashika fault around Bongna hills lava and agglomerate at Kawaba and Galu regions, and Wawa zones show possible uranium rich veins. Zona and Wawa areas, which have also been reported by Suh and Dada (1998) and Oshin and Rahaman (1986) to be rich in uranium and favourable for uranium deposition, were also found to have high uranium concentration. However, uranium depositions in the study area (rift-related basin) might

be low-grade due to multiple tectonic reactivation and re-precipitation of the ore (Haruna et al. 2012).

Conclusions

Results from the structural analysis of the aeromagnetic data showed that the study area is dissected by many structures that trend ENE–WSW, NE–SW, E–W, NNE–SSW, WNW–ESE, and NW–SE; among which the ENE–WSW and NE–SW trends dominate. These structures dip vertically, northeasterly, southwesterly, northwesterly, and southeasterly. The basement faults in the study area dominantly exist between the depths of 500 and 1000 m. The northwesterly and southeasterly dipping faults dip in the same direction as the paleocurrent direction (direction of depositions of sediments) and trend in a direction perpendicular to the direction of uranium deposition in the study area. These faults could, therefore, serve as potential traps for uranium deposition in the study area.

The result of this study has shown that the uranium ores were remobilized epigenetically from the granitic rocks and were re-deposited into sedimentary rocks (Bima sandstone formation). The depth to the basement was estimated to be between 150 and 1941 m below the flight line. The areas showing vein-type deposition were found in the Burashika Group (Bongna Hills) and Wawa area. The anatectic migmatite in the northeastern region and the uranium rich Bima formations in the study area show both fault/fracture and contact types of depositions. The structures in these identified formations are highly favourable for uranium mineralization in the study area.

The study, therefore, concluded that the studied area is dissected by several linear structures, among which the ENE–WSW and NE–SW trending structures dominate, and that the deposits of uranium ore in the studied area are likely to be found in: the Bima sandstones of Wade, Shinga, Bima Hill, Wuyo, Teli, Bryel, Dali, Barkan, Gasi, Kunkun, Boragara, Deba, and Gberundi localities; the anatectic migmatite at Kubuku, Whada, and Hyama; and the Bongna hills and agglomerates around Burashika, Kawaba, and Galu. However, these areas which are likely to be mineralized zones of uranium deposition are needed to be probed further for exploration purposes.

Compliance with ethical standards

Conflict of interest There is no conflict of interest in this research.

References

Anudu GK, Stephenson RA, Macdonald DM (2014) Using high resolution aeromagnetic data to recognise and map intra-sedimentary volcanic rocks and geological structures across the Cretaceous middle Benue Trough, Nigeria. Elsevier J Afr Earth Sci 99:625–636

Bell RT (1996) Sandstone uranium. Geology Survey of Canada, Geology of Canada, no 8, pp 212–219

Benkhelil J (1986) Geological map of part of the Upper Benue Valley; Explanatory Note. Elf Nigeria Ltd, p 4–16

Bowden P, Bennett JN, Kinnaird JA, Whitley JE, Abaa SI, Hadzigeorgiou-Stavrakis PK (1981) Uranium in the Niger-Nigeria younger granite province. Mineral Mag 44:379–389

Cambon AH (1994) Uranium deposits in granitic rocks. In: Notes on the national training course on uranium geology and exploration. IAEA and NMA, Cairo, Egypt, pp 8–20

Carter JD, Barber DFM, Tait EA (1963) The geology of parts of Adamawa, Bauchi and Bornu Provinces in Northeastern Nigeria. Bulletin of Geological Survey, Niamey, p 30

Clark SP, Peterman ZE, Heier KS (1966) Abundance of uranium, thorium and potassium. In Clarke SP Jr. (Ed), Handbook of physical constants, Geological Society of America. Memoir 97, Section 24, p 521–554

Darnley AG (1975) Geophysics in uranium exploration. Geological Survey of Canada, Uranium Exploration, Ottawa, pp 21–31

Dentith M (2011) Magnetic methods, airborne. In: Gupta HS (ed) Encyclopedia of solid earth geophysics, vol 1. Springer, Dordrecht, pp 761–766

Dobrin MB, Savit CH (1988) Introduction to geophysical prospecting, 4th edn. McGraw-Hill Books, New York, pp 633–725

Foote RS, Humphrey NB (1976) Airborne radiometric techniques and applications to Uranium exploration, Exploration for Uranium Ore (1AEA-SM 208/47). IAEA, Vienna

Funtua II, Okujeni CD (1996) Element distribution patterns in the uranium occurrence at Mika, northeastern Nigeria. Chem Erde 56:245–260

Gaafar I, Aboelkhair H (2014) Analysis of geological and geophysical datasets for radioelement exploration in KabAmiri area, central eastern desert. Egypt. Open Geol J 8(Suppl 1: M3):34–53

Guiraud M (1990) Tectono-sedimentary framework of the early Cretaceous continental Bima Formation (Upper Benue Trough, Northeastern Nigeria). J Afr Earth Sci 10:341–353

Haruna IV, Ahmed HA, Ahmed AS (2012) Geology and tectonosedimentary disposition of the Bima sandstone of the Upper Benue Trough (Nigeria): implications for sandstone-hosted Uranium deposits. J Geol Mining Res 4(7):168–173

Lauri LS, Turunen P (2015) Airborne radiometric data as a uranium exploration tool case studies from Southern Lapland. Geophysical Signatures of Mineral Deposit types in Finland, Geological Survey of Finland, Special Paper 58, pp 107–116

Maurin JC, Lancelot JR (1990) Structural setting and U-Pb dating of uranium mineralization from the north-eastern part of Nigeria (Upper Benue Region). J Afr Earth Sci 10:421–433

Nabighian MN (1972) The analytic signal of two dimensional magnetic bodies with polygonal crosssection: its properties and use for automated anomaly interpretation. Geophysics 37

Nabighian MN (1984) Toward a three-dimensional automatic interpretation of potential field data via generalised Hilbert transforms: fundamental relations. Geophysics 49:780–789

Ndougsa-Mbarga T, Feumoe ANS, Manguelle-Dicoum E, Fairhead JD (2012) Aeromagnetic data interpretation to locate buried faults in South East Cameroon. Geophysica 48(1–2):49–63

Nwajide CS (2013) Geology of Nigeria's sedimentary basins. CSS Bookshop Limited, First Published, ISBN 978-978-8401-67-4, pp 27–110

Nwosu OB (2014) Determination of magnetic basement depth over parts of middle Benue Trough by Source Parameter Imaging (SPI) technique using HRAM. Int J Sci Technol Res 3(1):262–271

Obaje NG (2009) Geology and mineral resources of Nigeria. Springer, Berlin, pp 2, 49–65

Obiora SC (2009) Field measurements in descriptions of igneous and metamorphic rocks. In: Lambert-Aikhionbare DO, Olayinka AI (eds) Proceedings of field mapping standardisation workshop, Ibadan University Press, Ibadan, pp 105–125

Odebode MO (2010) A handout on the Geology of the Benue and Anambra Basin, Nigeria (unpublished work)

Oshin IO, Rahaman MA (1986) Uranium favourability study in Nigeria. J Afr Earth Sci 5(2):167–175

Philips JD (2000) Locating magnetic contacts: a comparison of the horizontal gradient, analytic signal, and local wavenumber methods: Calgary. In: 70th Meeting, society of exploration geophysicists, expanded abstracts with biographies, 2000 Technical Program, vol 1, pp 402–405

Reid AB, Allsop JM, Granser H, Millet AJ, Somerton IW (1990) Magnetic interpretation in three dimensions using Euler deconvolution. Geophysics 55:80–91

Roest W, Verhoef J, Pilkington M (1992) Magnetic interpretation using 3-D analytical signal. Geophysics 57:116–125

Ruzicka V (1975) New sources of uranium? Types of uranium deposits presently unknown in Canada. Geological Survey of Canada, Uranium Exploration 75, pp 13–47

Ruzicka V (1992) Types of uranium deposits in the former U.S.S.R.; Colorado School of Mines Quarterly Review 92(1):19–27

Sambo AS (2008) Matching electricity supply with demand in Nigeria. In: Paper presented at the "National Workshop on the Participation of State Governments in the Power Sector: Matching Supply with Demand", 29 July 2008, LadiKwali Hall, Sherato Hotel and Towers, Abuja

Saunders DF, Potts MJ (1976) Interpretation and application of high sensitivity airborne gamma ray spectrometer data; in Exploration for Uranium Ore Deposits. Proc. Series, IAEA, Vienna, pp 107–125

Suh CE, Dada SS (1998) Mesostructural and microstructural evidences for a two stage tectono-metallogenetic model for the uranium deposit at Mika, northeastern Nigeria: a research note. Nonrenew Resour 7(1):75–83

Suh CE, Dada SS, Ajayi TR, Matheis G (1998) Integrated structural and mineral alteration study of the Zona uranium anomaly, northeast Nigeria. J Afr Earth Sci 27(1):129–140

Tauchid M (1993) Nuclear raw Materials: developing resources through technical cooperation. Int Atom Energy Agency Bull 35:14–17

Telford WM, Geldart LP, Sheriff RE (1990) Applied geophysics, 2nd edn. Cambridge University Press, Cambridge, pp 62–123, 611–636

Thompson DT (1982) EULDPH: a new technique for making computer-assisted depth estimates from magnetic data. Geophysics 47:31–37

Thurston JB, Smith RS (1997) Automatic conversion of magnetic data to depth, dip, and susceptibility contrast using the SPI method. Geophysics 62:807–813

Thurston JB, Guillon C, Smith R (1999) Model independent depth estimation with the SPITM method. In: 69th Annual International Meeting, SEG, Expanded Abstracts, pp 403–406

Thurston JB, Smith RS, Guillon JC (2000) A multi-model method for depth estimation from magnetic data. Geophysics 67:555–561